

Stress-induced cavitation for the streaming motion of a viscous liquid past a sphere

By **J. C. PADRINO¹, D. D. JOSEPH^{1†}, T. FUNADA²
J. WANG¹ AND W. A. SIRIGNANO³**

¹Department of Aerospace Engineering and Mechanics, University of Minnesota, Minneapolis, MN 55455, USA

²Department of Digital Engineering, Numazu College of Technology, Ooka 3600, Numazu, Shizuoka, 410-8501, Japan

³Department of Mechanical and Aerospace Engineering, University of California, Irvine, CA 92697, USA

(Received May 2006)

The theory of stress-induced cavitation is applied here to the problem of cavitation of a viscous liquid in the streaming flow past a stationary sphere. This theory is a revision of the pressure theory which states that a flowing liquid will cavitate when and where the pressure drops below a cavitation threshold, or breaking strength, of the liquid. In the theory of stress-induced cavitation the liquid will cavitate when and where the maximum tensile stress exceeds the breaking strength of the liquid. For example, liquids at atmospheric pressure which cannot withstand tension will cavitate when and where additive tensile stresses due to motion exceed one atmosphere. A cavity will open in the direction of the maximum tensile stress which is 45° from the plane of shearing in pure shear of a Newtonian fluid. This maximum tension criterion is applied here to analyze the onset of cavitation for the irrotational motion of a viscous fluid, the special case imposed by the limit of very low Reynolds numbers and the fluid flow obtained from the numerical solution of the Navier–Stokes equations. The analysis leads to a dimensionless expression for the maximum tensile stress as a function of position which depends on the cavitation and Reynolds numbers. The main conclusion is that at a fixed cavitation number the extent of the region of flow at risk to cavitation increases as the Reynolds number decreases. This prediction that more viscous liquids at a fixed cavitation number are at greater risk to cavitation seems not to be addressed, affirmed or denied, in the cavitation literature known to us.

1. Introduction

Winer & Bair (1987) and, independently, Joseph (1995, 1998) proposed the maximum tension criterion for cavitation which states that the flowing liquid will cavitate if the maximum tensile stress exceeds a critical value. Since this maximum stress is associated with a principal direction, this criterion is not isotropic. Winer & Bair (1987) introduced the idea that stress-induced cavitation may enter into the apparent shear thinning of liquid lubricants. They remarked that shear thinning may be the result of a yielding or cavitation event that takes place at a critical value of the liquid's tensile stress. They further note that 'for some high shear rate viscosity data at atmospheric pressure the

† Corresponding author: Tel.: +1-612-626-8000; fax: +1-612-626-1558. E-mail address: joseph@aem.umn.edu (D.D. Joseph).

principal normal stress may approach quite low values relative to one atmosphere suggesting the possibility of cavitation or fracture of the material resulting in a reduced shear stress'. In a private communication, Prof. Bair noted that '...There was little interest from tribologists, so we dropped it until recently. In the original work we were able to see to the voids by eye using a clear plastic outer cylinder...'.

The maximum tension criterion is embedded as one possibility for liquid failure presented by analysis of the state of stress in Joseph's theory. A comparison of these two theories can be found in the study of cavitation in creeping shear flows by Kottke, Bair and Winer (2005). Numerous examples of cavitation in shear flow by other researchers are discussed by Kottke *et al.* (2005). Examples of stress-induced cavitation in extensional flow and shear flow were discussed by Joseph (1998). Pereira *et al.* (2001) did a theoretical study of cavitation in a journal bearing with axial throughput. They found that the inception of cavitation in a moving fluid is always stress induced. Funada *et al.* (2006) carried out an analysis of stress induced cavitation in a two-dimensional aperture flow modeling atomizers in which cavitation is well documented. The aperture flow was expressed using a complex potential and the stress calculated using viscous potential flow. They found that the viscous stress was huge near the tips of the aperture, thus cavitation could be induced. The region at risk to cavitation is larger, for a fixed cavitation number, when the Reynolds number is smaller.

In this paper, we study stress-induced cavitation in the streaming motion past a sphere. This kind of study differs from the typical one based solely upon the local pressure; it is necessary to compute the field of principal stresses as well as the pressure. This program is carried, without approximation, by numerical simulation of the Navier-Stokes equations. We also analyze the same problem for two cases in which simple explicit formulas for cavitation inception may be derived. The first case, Stokes flow, is an asymptotic limit in which inertia – the Reynolds number – is not in play. In the general case, in which inertia is important, the criterion for cavitation inception is a relation between the cavitation number and the Reynolds number; the region at risk to cavitation increases when the cavitation number increases and the Reynolds number decreases. This dependence is shown explicitly by the analysis based on potential flow of a viscous fluid (VPF) presented in §5 and by the numerical simulation of the Navier-Stokes equation presented in §6.

2. Theory of stress-induced cavitation

The stress in an incompressible Newtonian fluid is given by

$$\mathbf{T} = -p\mathbf{1} + 2\mu\mathbf{D}[\mathbf{u}], \quad (2.1)$$

where $\mathbf{D}[\mathbf{u}]$ is the symmetric part of the velocity gradient, \mathbf{u} is the velocity field and $\text{tr}\mathbf{D}[\mathbf{u}] = 0$, such that

$$\text{tr}\mathbf{T} = T_{11} + T_{22} + T_{33} = -3p. \quad (2.2)$$

We define the stress at the cavitation threshold as p_c . It is positive when compressive and negative when tensile. Classically, the vapor pressure is taken as the threshold stress; however, in the next section, we discuss examples where different values, including tensile values, should be used for the cavitation threshold.

In the pressure criterion, the viscous part of the stress tensor is not considered and the liquid will cavitate when

$$-p + p_c > 0. \quad (2.3)$$

The pressure criterion assumes that cavitation inception is determined by the average

stress, called the pressure. The fluid cannot average its stresses; it sees only principal stresses and when the actual state of stress is considered there is at least one stress which is more compressive and another which is more tensile than the average stress. The most conservative criterion is the one which requires that the most compressive stress is larger than the cavitation threshold; suppose T_{22} is the most compressive and T_{11} is the most tensile (or least compressive) stress, then if

$$T_{22} + p_c > 0 \quad (2.4)$$

for cavitation, it will surely be true that

$$-p + p_c > 0 \text{ and } T_{11} + p_c > 0. \quad (2.5)$$

The maximum tension theory, which perhaps embodies the statement that liquids which are not specially prepared will cavitate when they are subject to tension, can be expressed by the condition that supposing T_{11} to be the maximum of the three principal stresses,

$$T_{11} + p_c > 0. \quad (2.6)$$

The cavitation number K compares the cavitation threshold p_c with a typical pressure; here in our sphere problem, with the pressure p_∞ at infinity. We define

$$K = \frac{p_\infty - p_c}{N_R} \quad (2.7)$$

where $N_R = \mu U/L$ for Stokes flow and $N_R = \rho U^2/2$ when inertia acts; L is a characteristic length scale. Later, the analysis will show that the stress difference between the free-stream pressure and the cavitation threshold $p_\infty - p_c$ is the critical value rather than the cavitation threshold by itself.

The maximum tension criterion (2.6) has recently been studied in a numerical simulation of bubble growth in Newtonian and viscoelastic filaments undergoing stretching by Foteinopoulou *et al.* (2004). They base their analysis on the Navier-Stokes equations for Newtonian fluids and the Phan-Thien/Tanner model for viscoelastic fluids. They compute the principal stresses and evaluate the cavitation threshold for the maximum tension criterion (2.6), the pressure theory (2.3) and the minimum principal theory (2.4). They find that the capillary number at inception is smallest for (2.6). As remarked by Kottke *et al.* (2005), the cavitation threshold p_c could be negative or positive. In the case of $p_c < 0$, the liquid shows tensile strength; for $p_c = 0$, a cavity will open if the maximum principal stress becomes positive (i.e., tensile), and, if $p_c > 0$, the cavitation threshold is given by a positive pressure (i.e., compressive stress). The latter case is typified by the pressure theory of cavitation determined by the local pressure dropping below the vapor pressure.

To each principal stress there corresponds a principal direction, which plays a role in the physics of cavity inception. Joseph (1998) asserts that 'if a cavitation bubble opens up, it will open in the direction of maximum tension. Since this tension is found in the particular coordinate system in which the stress is diagonal, the opening direction is in the direction of maximum extension, even if the motion is a pure shear. It may open initially as an ellipsoid before flow vorticity rotates the major axis of ellipsoid away from the principal tension axis of stress, or it may open abruptly into a 'slit' vacuum cavity perpendicular to the tension axis before vapour fills the cavity as in the experiments of Kuhl *et al.* (1994)'. These ideas are illustrated in cartoons showing the orientation of the principal directions on the surface of the sphere for each approach considered in this study.

Consider the expression for the stress tensor for a Newtonian fluid given in (2.1).

Adding the diagonal tensor $p_c \mathbf{1}$ to both sides and decomposing $p = p_\infty + p^*$ yields

$$\mathbf{T} + p_c \mathbf{1} = -(p_\infty - p_c) \mathbf{1} - p^* \mathbf{1} + 2\mu \mathbf{D}. \quad (2.8)$$

Dividing through by the normalizing factor N_R , (2.8) becomes

$$\frac{\mathbf{T} + p_c \mathbf{1}}{N_R} = -\left(K + \frac{p^*}{N_R}\right) \mathbf{1} + \frac{2\mu}{N_R} \mathbf{D}. \quad (2.9)$$

The strain-rate tensor can be readily diagonalized. Thus the principal stresses and directions can be determined. Suppose now that $K = K_c$ at the marginal state separating cavitation from no cavitation. For shortness, let us call K_c the incipient cavitation number. This marginal state is defined by an equality in one of the three criteria (2.3), (2.4) or (2.6). For the maximum tension theory $K = K_c$ when $T_{11} + p_c = 0$. In particular, for the maximum principal stress T_{11} , (2.9) yields

$$(T_{11} + p_c)/N_R = -(K + p^*/N_R) + 2\mu D_{11}/N_R, \quad (2.10)$$

where D_{11} denotes the maximum principal rate of strain. Then, $K_c = (-p^* + 2\mu D_{11})/N_R$ is, in general, a scalar function of the position in the fluid domain. For a positive cavitation number, consider $K = K_c + K^*$ such that $(T_{11} + p_c)/N_R = -K^*$. It is thus clear from (2.10) that

$$T_{11} + p_c < 0 \text{ when } K > K_c, \quad (2.11)$$

and

$$T_{11} + p_c > 0 \text{ when } K < K_c. \quad (2.12)$$

The latter condition implies that the liquid is at the most risk to cavitation in regions where $K < K_c$. For instance, for a fixed cavitation number K , no cavity will open if $K > K_{c,\max}$, the maximum value that K_c takes in the entire fluid domain. On the other hand, the cavitation number K based on the actual hydrodynamics, may vary in the fluid domain, since the cavitation threshold p_c may also change with position. For example, Singhal *et al.* (2002) included in their cavitation model the effect of the local turbulence pressure fluctuations in the phase-change threshold pressure.

3. Cavitation threshold

Cavitation can be defined as the formation, expansion and collapse of a cavity in a liquid. In general, the ‘formation’ of a cavity implies both the appearance of a new void or the growth of a preexisting nucleus beyond a critical size large enough to be observed with the unaided eye (Young, 1989). The idea of the opening of a cavity in the liquid continuum brings into consideration the concept of liquid tensile strength, which is a material property. The pressure criterion for cavitation states that the liquid cavitates when the local pressure reaches the vapor pressure somewhere in the domain. Knapp, Daily & Hammit (1970) discusses that, although the inception of a cavity has been observed in experiments when local pressure is near the vapor pressure, deviations of various degrees have been reported for different liquids such that the results do not agree with the vapor pressure criterion. Knapp *et al.* define the vapor pressure as ‘the equilibrium pressure, at a specified temperature, of the liquid’s vapor which is in contact with an *existing* free surface.’ They argue that the stress required to rupture the continuum in a homogeneous liquid is determined by the tensile strength, not by the vapour pressure. The literature on the tensile strength of liquids is vast and a good account of experimental results is given in the book by Knapp *et al.* (1970) for various liquids. In particular for

water, values ranging from 13 to 200 atm are listed. Briggs (1950) reports inception of cavities in water induced by centrifugal force for pressures between vapor pressure and -300 atm (tension). Recently, Kottke, Bair & Winer (2003) measured the tensile strength of nine liquids, including water, lubricant and polymeric liquids. Theoretical estimates of the tensile strength of water render large negative values in the interval -500 atm to -10,000 atm, which, however, have never been reported from experiments (Strassberg, 1959). Both observed phenomena, the wide scatter of the experimental results and the inception of cavitation at pressures much higher than the theoretical tensile strength reported in the literature indicate the existence of weak spots in the fluid that allows breaking of the continuum. Plesset (1969) comments that bubbles can grow to macroscopic dimensions starting from voids of size already beyond the molecular level under tensile stresses much lower than the theoretical values predicted for pure liquids.

Fisher (1948) reasons that, in a similar manner as very greatly subcooled liquids (such as glass) may fail by the nucleation and growth of a crack, a fluid may fail under tension by the growth of a cavity starting from very small holes. By applying methods of nucleation theory, Fisher predicts fracture tensions for several liquids with values, however, one order of magnitude higher than the experimental evidence. Some mechanism is required to stabilize preexisting nuclei in the liquid. For a very small bubble suspended in the liquid, the pressure inside the bubble is much higher than the pressure in the surrounded liquid because of surface-tension forces. This pressure difference diffuses the gas out of the gas void until it vanishes. On the other hand, bubbles not so small will rise and escape through the surface. Harvey and collaborators (1944a) introduced the idea of stabilized gas pockets attached to submicroscopic and hydrophobic crevices in the surface of the liquid container or in solid impurities. The size of these nuclei can be of the order of microns. Harvey *et al.* (1944b) supported their theory with results from a series of experiments in which previously pressurized and unpressurized samples of water were boiled at atmospheric pressure such that the saturation pressure corresponding to the boiling temperature was taken as a rough measure of the effective tensile strength. Although quite broad scatter was observed in the results for the pressurized samples, they all boiled at temperatures much higher than the saturation temperature for atmospheric pressure, which was the boiling temperature showed by the unpressurized samples. Tensile strength of 16 atm were reported in some samples previously pressurized.

Harvey *et al.* (1947) performed a different type of experiments to investigate tensile strength of water by high-speed removal of a squared-ended glass rod from a narrow glass tube containing the liquid. Meticulous cleaning of the glass surfaces and pressurization of the sample with the rod in position were done to remove hydrophobic spots and gas nuclei. In terms of the rod-withdrawal speed, they found that 'if the rod surface contained glass nuclei, or was hydrophobic and free of gas nuclei, cavitation occurred at the rear end when the velocity was less than 3 m/s, but if completely hydrophilic and free of gas nuclei, the velocity could be 37 m/s (...) without cavitation.' Knapp (1958) confirmed Harvey's results performing experiments at a rather larger scale. Strasberg (1959) explored the onset of acoustically-induced cavitation in tap water finding that microscopic undissolved air cavities, which show a slow motion toward the surface, play an important role as nuclei. Apfel (1970) extended Harvey's theory to consider the condition required in a liquid for the inception of a vapor cavity from a solid impurity in the liquid. Crum (1970) examined the crevice model of Harvey *et al.* comparing its predictions with experimental evidence.

From the standpoint of hydrodynamic cavitation, stream nuclei carried by the moving liquid as particulates or microbubbles have a greater contribution as sites for onset of cavitation than the surface nuclei originated in crevices or cracks on the solid boundaries

(Billet 1985 and references therein). Turbulence has been shown to influence cavitation inception and its effect has been accounted for in models through the phase-change threshold (Singhal *et al.* 2002).

The inception of a cavity can be an abrupt event, where the liquid must rupture, instead of a continuous one. Chen & Israelachvili (1991) and Kuhl *et al.* (1994) monitored the elastohydrodynamic deformations of two curve surfaces that move relative to each other separated by a thin–liquid film of nanoscopic dimensions. A low molecular weight polymer liquid of polybutadiene and bare mica smooth surfaces having strong adhesion to the liquid were utilized in the tests. When the surfaces move normally with a slow separation speed they bulge outward becoming pointed at the location of the shortest surface separation. This shape indicates the existence of a tensile stress acting on the surface. If the separation speed is increased beyond a critical value, a vapor cavity opens in the liquid at the position of the shortest separation, reducing the tensile stress, while the pointed surfaces suddenly recover their original shape. Chen & Israelachvili (1991) also used surfactant-coated mica surfaces, which have weak adhesion to the liquid, resulting in cavity formation at the liquid–solid interface. Kuhl *et al.* (1994) considered lateral sliding of a curved surface over a mostly plane surface with a thin liquid film in between. Describing the shape of the sliding element, they observed that ‘the leading edge becomes more rounded and lifts off while the trailing edge becomes more pointed.’ For a sliding speed larger than some critical value, the pointed trailing edge snaps back, while a small cavity opens in the wake.

Cavitation inception has been observed in liquids undergoing shearing, suddenly changing the rheological response of the samples. Bair and Winer (1990) inferred cavitation inception by detecting yielding of a synthetic oil during rheological tests using a rotating concentric cylinder rheometer for a shear stress near the hydrostatic pressure (1.73 MPa). A similar phenomenon was noticed by Bair and Winer (1992) for polybutene in simple shear at low pressures (0.1 to 1 MPa) for a shear stress of 0.075 MPa in excess of the internal absolute pressure. This magnitude may represent the amount of tension that this liquid can resist without the opening of a cavity. Archer, Ternet & Larson (1997) visualized the opening of bubbles within a sample of low-molecular-weight polystyrene subjected to start-up of steady shearing flow. They noticed that bubbles seemed to appear near dust particles. As a consequence of cavitation, the shear stress abruptly drops after it reaches a maximum of 0.1 MPa. Kottke *et al.* (2005) observed the inception of cavities in polybutene undergoing shearing tests using a Couette viscometer. Cavities become visible when the measured shear stress matches the ambient pressure. According to their principal normal stress cavitation criterion (PNSCC), this result implies that the sample liquid is not able to withstand tension. They suggest that cavitation grows from preexisting nuclei stabilized in some cracks or crevices on the solid boundaries.

The previous survey has shown that the idea of minute gas and vapor pockets in the liquid acting as nucleation sites is plausible and generally accepted. Nevertheless, a precise definition of the cavitation threshold and a clear description of the wide gamut of factors that influence this critical value is yet to be accomplished. We use the words ‘cavitation threshold’ and ‘breaking strength’ as synonymous with the threshold at which the liquid continuum will fracture. This threshold can vary from place to place in a sample. The threshold need not be a material parameter. In the case of heterogeneous nucleation, the cavitation threshold depends on the sample preparation, the density and nature of nucleation sites. In the case of homogeneous nucleation, the threshold may be taken as the vapor pressure. The vapor pressure is a thermodynamic quantity which is defined for uniform isotropic samples for which the stress tensor is isotropic; for static samples, bubble nucleation is a function of pressure and nothing else. In this paper, the cavitation

threshold, p_c , is not necessarily the vapor pressure; this value is regarded as given and is not a subject for study here. For liquid which cannot withstand tension, $p_c = 0$.

In sections 4, 5 and 6 we discuss three parallel solutions approaches using the maximum tension criterion, namely, Stokes flow, viscous potential flow and the numerical solution of the incompressible Navier–Stokes equations, which can be read in any order.

4. Cavitation of Stokes flow

The problem of heterogeneous nucleation of bubbles in the creeping flow of a viscous liquid sheared between parallel plates has been considered by Kottke, Bair & Winer (2005). They find good agreement between experiments and cavitation based on the maximum tension criterion. These authors indicate:

Liquid failure has been observed in low Reynolds number (Stokes) shear flows where reduction of the hydrodynamic pressure should not occur. Cavitation in Stokes flows has implications in lubrication, polymer processing, and rheological measurements. Such cavitation can be predicted by a principal normal stress cavitation criterion (PNSCC). We present results of a direct experimental test of the PNSCC. Imaging of the cavitation events suggests that the cavitation is gaseous and originates from preexisting nuclei. Crevice-stabilized gas nuclei are assumed, and numerical simulations are used to investigate the cavitation event for a Newtonian liquid. The inception of cavitation from a preexisting nucleus, the persistence of suitable nuclei, and the growth and deformation of shed bubbles are considered.

Ashmore, del Pino & Mullin (2005) study the Stokesian fluid dynamics around a sphere free to move inside a rotary cylinder filled with viscous liquid, showing that the inception of cavitation breaks the symmetry of the flow field, creating a net normal force that prevents contact between the sphere and the boundary. We analyze in this section stress-induced cavitation when the stream is creeping in the Stokes flow limit. A cartoon of the flow is given in figure 1 using spherical–polar coordinates, showing the angle α , which sets the stresses into principal directions. For this type of fluid motion, the principal strain–rates and stresses and their corresponding principal directions can be determined. The velocity and pressure fields for Stokes flow past a sphere are given by the expressions

$$u_r = U \left[1 - \frac{3}{2} \frac{a}{r} + \frac{1}{2} \frac{a^3}{r^3} \right] \cos \theta, \quad u_\theta = -U \left[1 - \frac{3}{4} \frac{a}{r} - \frac{a^3}{4r^3} \right] \sin \theta, \quad (4.1)$$

$$p = p_\infty - \frac{3\mu a U}{2r^2} \cos \theta. \quad (4.2)$$

The components of the viscous stress tensor $2\mu\mathbf{D}[\mathbf{u}]$ with respect to the spherical polar reference frame of figure 1 are determined using (4.1) and the formulae

$$\begin{aligned} D_{rr} &= \frac{\partial u_r}{\partial r}, & D_{\theta\theta} &= \left(\frac{1}{r} \frac{\partial u_\theta}{\partial \theta} + \frac{u_r}{r} \right), \\ D_{\varphi\varphi} &= \left(\frac{u_r}{r} + \frac{u_\theta}{r} \cot \theta \right), & D_{r\theta} &= \frac{1}{2} \left[r \frac{\partial}{\partial r} \left(\frac{u_\theta}{r} \right) + \frac{1}{r} \frac{\partial u_r}{\partial \theta} \right]. \end{aligned} \quad (4.3)$$

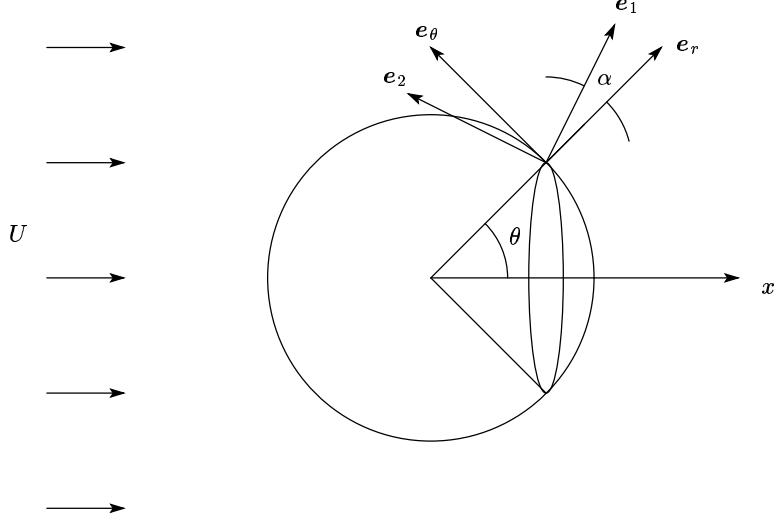


FIGURE 1. Streaming flow of a liquid past a sphere of radius a . The spherical-polar coordinates basis vectors that lie in the plane of motion are shown. The angle α puts the stresses into principal axes.

Thus, the viscous stress tensor $2\mu\mathbf{D}[\mathbf{u}]$ may be written in matrix form as

$$2\mu \begin{bmatrix} D_{rr} & D_{r\theta} & 0 \\ D_{r\theta} & D_{\theta\theta} & 0 \\ 0 & 0 & D_{\varphi\varphi} \end{bmatrix} = \frac{3}{2}\mu U \frac{a^3}{r^4} \begin{bmatrix} 2\left[\left(\frac{r}{a}\right)^2 - 1\right] \cos\theta & -\sin\theta & 0 \\ -\sin\theta & -\left[\left(\frac{r}{a}\right)^2 - 1\right] \cos\theta & 0 \\ 0 & 0 & -\left[\left(\frac{r}{a}\right)^2 - 1\right] \cos\theta \end{bmatrix}, \quad (4.4)$$

which is rotated by an angle α to obtain its diagonalized form

$$\frac{3}{2}\mu U \frac{a^3}{r^4} \begin{bmatrix} \frac{1}{2}\left[\left(\frac{r}{a}\right)^2 - 1\right] \cos\theta - \frac{\sin\theta}{\sin 2\alpha} & 0 & 0 \\ 0 & \frac{1}{2}\left[\left(\frac{r}{a}\right)^2 - 1\right] \cos\theta + \frac{\sin\theta}{\sin 2\alpha} & 0 \\ 0 & 0 & -\left[\left(\frac{r}{a}\right)^2 - 1\right] \cos\theta \end{bmatrix}. \quad (4.5)$$

The angle of rotation α is related to the polar angle θ by the expression

$$\cot 2\alpha = -\frac{3}{2} \left[\left(\frac{r}{a}\right)^2 - 1 \right] \cot\theta \quad (4.6)$$

Expression (4.6) can be solved to find the rotation angle α ($-0.5 \leq \alpha/\pi \leq 0.5$) required to rotate the polar coordinates (r, θ) such that the direction defined by the unit vector \mathbf{e}_r coincides with the principal direction associated with the most tensile (or the least compressive) principal stress on the plane of motion. The orientation of the principal axes on the surface of the sphere $r = a$ in the plane of motion is illustrated in figure 2.

Expression (2.1) can be modified by adding $p_c\mathbf{1}$ to both sides and substituting (4.2) for the pressure p and (4.5) for the viscous stress $2\mu\mathbf{D}$. Defining the cavitation number

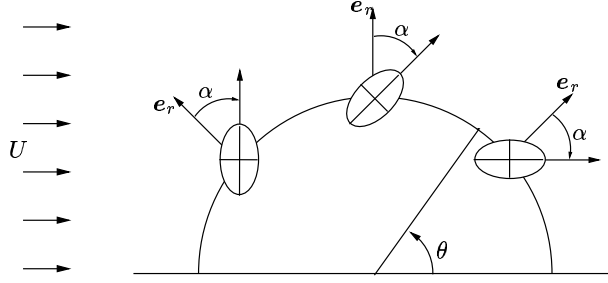


FIGURE 2. Schematic view of the orientation of the principal directions in the plane of motion from the Stokes flow analysis (4.6) on the surface of the sphere. In this case, $\alpha = -45^\circ$ for all θ . The major axis in the ellipse represents the maximum tensile stress. The angle α puts the direction defined by the unit outward normal vector e_r into the principal direction of the maximum tensile stress.

and the Reynolds number, respectively, as

$$K = \frac{p_\infty - p_c}{\mu U/a}, \quad (4.7)$$

and

$$Re = \frac{\rho U a}{\mu}, \quad (4.8)$$

the following expression results after arranging

$$\begin{aligned} \frac{\mathbf{T} + p_c \mathbf{1}}{\frac{\mu U}{a}} &= - \left[K - \frac{3}{2} \left(\frac{a}{r} \right)^2 \cos \theta \right] \begin{bmatrix} 1 & 0 & 0 \\ 0 & 1 & 0 \\ 0 & 0 & 1 \end{bmatrix} + \\ &+ \frac{3}{2} \left(\frac{a}{r} \right)^4 \begin{bmatrix} \frac{1}{2} \left[\left(\frac{r}{a} \right)^2 - 1 \right] \cos \theta - \frac{\sin \theta}{\sin 2\alpha} & 0 & 0 \\ 0 & \frac{1}{2} \left[\left(\frac{r}{a} \right)^2 - 1 \right] \cos \theta + \frac{\sin \theta}{\sin 2\alpha} & 0 \\ 0 & 0 & - \left[\left(\frac{r}{a} \right)^2 - 1 \right] \cos \theta \end{bmatrix}. \end{aligned} \quad (4.9)$$

Since the right hand side is diagonal, (4.9) gives the principal stresses. Not surprisingly, this expression is independent of the Reynolds number. For the Stokes flow solution given in (4.9), one can show that at any point the most tensile (least compressive) and most compressive (least tensile) principal stresses lie on the plane of motion. Suppose that for a point (r, θ) in the fluid domain, T_{11} is the maximum of the three principal stresses. Then, the maximum tension criterion for cavitation (2.6) can be applied to this fluid motion. Let K_c be the cavitation number in the marginal state determined by $T_{11} + p_c = 0$, then (4.9) gives rise to a functional relation $K_c = f(r, \theta)$, from which a contour plot with lines of constant K_c can be readily obtained.

For fluid motions in which inertia effects are dominant, it is customary to use the dynamic pressure, $\rho U^2/2$, as the normalization factor for pressure. For the purpose of analysis, one may wish to compare results from creeping flows with results from fluid motions with higher Reynolds numbers. In such a case, the following relations can be useful,

$$\frac{p_\infty - p_c}{\mu U/a} = \frac{Re}{2} \frac{p_\infty - p_c}{\frac{1}{2} \rho U^2}, \quad (4.10)$$

for the cavitation number and,

$$\frac{\mathbf{T} + p_c \mathbf{1}}{\mu U/a} = \frac{Re}{2} \frac{\mathbf{T} + p_c \mathbf{1}}{\frac{1}{2} \rho U^2}, \quad (4.11)$$

for the stress tensor. Thus the quantities defined in terms of the viscous forces scale with their counterpart defined in terms of the dynamic pressure by a factor of $Re/2$ everywhere in the fluid domain.

Lines of constant K_c for the marginal state of cavitation according to (4.9) are presented in §7 and compared with solutions from direct numerical simulation and viscous potential flow for $Re = 0.01$ (see figure 9).

In particular, on the surface of the sphere, $r = a$, (4.9) reduces to

$$\begin{bmatrix} T_{11} + p_c & 0 & 0 \\ 0 & T_{22} + p_c & 0 \\ 0 & 0 & T_{33} + p_c \end{bmatrix} / (\mu U/a) = -K \begin{bmatrix} 1 & 0 & 0 \\ 0 & 1 & 0 \\ 0 & 0 & 1 \end{bmatrix} + \frac{3}{2} \begin{bmatrix} \cos \theta + \sin \theta & 0 & 0 \\ 0 & \cos \theta - \sin \theta & 0 \\ 0 & 0 & \cos \theta \end{bmatrix} \quad (4.12)$$

It is shown in Appendix A that the maximum of K under the condition $T_{11} + p_c = 0$ occurs at $\theta = 45^\circ$. Therefore, the position $r = a$, $\theta = 45^\circ$ is the location most vulnerable to cavitation.

The principal axes representation of this tensor is achieved for $\alpha = -45^\circ$, which satisfies (4.6) for $r = a$. Expression (4.12) can be used to form the cavitation criteria. The maximum tension is achieved at $\theta = 45^\circ$. From the right-hand side of (4.12) it can be noticed that $T_{11} \geq T_{33} \geq T_{22}$ for the array shown in its left-hand side for all $0 \leq \theta \leq \pi$ since $\sin \theta \geq 0$ for this interval. This trend is presented in §7 (figure 12) where K_c versus θ/π have been plotted for the three principal stresses on the surface of the sphere for $Re = 0.01$.

5. Irrotational flow of a viscous fluid

Kuhn de Chizelle, Ceccio & Brennen (1995) studied the interactions between a travelling cavity and the potential flow exterior to the thin boundary layer around an axisymmetric headform. Liu & Brennen (1998) presented a mechanistic model for hydrodynamic cavitation event rate for flow over a headform that utilizes the pressure distribution given by potential flow modified to accommodate boundary layer effects. There is no literature other than the paper of Funada *et al.* (2006) on analysis of stress-induced cavitation using potential flow. The analysis of this problem, given below, is completely transparent; the effects of vorticity on cavitation on a solid sphere are mainly associated with the formation of wakes and the displacement of the region of irrotational flow (see §6). Considering the irrotational flow of a viscous fluid, the principal strain-rates and stresses and their corresponding principal directions can be determined. Then, the maximum tension criterion is applied to evaluate the cavitation threshold. The theory of viscous potential flow considered here includes the viscous components in the definition of the state of stress in the flowing liquid.

Irrotational flows of incompressible viscous fluids satisfy the Navier-Stokes equations and give rise to the usual Bernoulli equation because

$$\mu \nabla^2 \mathbf{u} = \mu \nabla \nabla^2 \phi = 0, \quad (5.1)$$

no matter what the value of μ . The stresses are given by

$$\mathbf{T} = -p\mathbf{1} + 2\mu\nabla \otimes \nabla\phi = \frac{1}{3}\text{Tr}(\mathbf{T})\mathbf{1} + 2\mu\nabla \otimes \nabla\phi, \quad (5.2)$$

where p is the average stress given by (2.2).

The flow is axisymmetric and steady and the potential $\phi(r, \theta)$ satisfies $\nabla^2\phi = 0$. In this analysis, spherical-polar coordinates as shown in figure 1 are utilized.

The potential for this flow is

$$\phi = U \left(r + \frac{1}{2} \frac{a^3}{r^2} \right) \cos\theta. \quad (5.3)$$

The velocity $\mathbf{u} = \mathbf{e}_r u_r + \mathbf{e}_\theta u_\theta$ is given by

$$u_r = \frac{\partial\phi}{\partial r} = U \left(1 - \frac{a^3}{r^3} \right) \cos\theta, \quad u_\theta = \frac{1}{r} \frac{\partial\phi}{\partial\theta} = -U \left(1 + \frac{1}{2} \frac{a^3}{r^3} \right) \sin\theta. \quad (5.4)$$

Note that the no-slip condition must be relaxed for viscous potential flow. So, the boundary layer is not resolved. The pressure is given by

$$\begin{aligned} p &= p_\infty + \rho \frac{U^2}{2} - \frac{\rho}{2} (u_r^2 + u_\theta^2) \\ &= p_\infty + \rho \frac{U^2}{2} \left[1 - \left(1 - \frac{a^3}{r^3} \right)^2 \cos^2\theta - \left(1 + \frac{1}{2} \frac{a^3}{r^3} \right)^2 \sin^2\theta \right], \end{aligned} \quad (5.5)$$

where p_∞ is the constant value of the pressure at infinity. The non-zero components of the viscous stress

$$2\mu\mathbf{D}[\nabla\phi] \quad (5.6)$$

are determined using the standard formulae (4.3) and the velocity field (5.4). This yields to the matrix of components

$$2\mu \begin{bmatrix} D_{rr} & D_{r\theta} & 0 \\ D_{r\theta} & D_{\theta\theta} & 0 \\ 0 & 0 & D_{\varphi\varphi} \end{bmatrix} = 3\mu U \frac{a^3}{r^4} \begin{bmatrix} 2\cos\theta & \sin\theta & 0 \\ \sin\theta & -\cos\theta & 0 \\ 0 & 0 & -\cos\theta \end{bmatrix}, \quad (5.7)$$

which can be rotated into diagonal form through an angle α satisfying

$$\tan 2\alpha = \frac{2}{3} \tan\theta. \quad (5.8)$$

From (5.8) we look for the angle α that puts by rotation with axis \mathbf{e}_φ the direction given by the unit vector \mathbf{e}_r into the principal direction corresponding to the most tensile (or the least compressive) principal stress in the plane of the motion. Without lack of generality, we consider this angle α to be in the interval $-0.5 \leq \alpha/\pi \leq 0.5$.

The diagonal form of $2\mu\nabla \otimes \nabla\phi$ is given by

$$3\mu U \frac{a^3}{r^4} \begin{bmatrix} \frac{1}{2}\cos\theta + \frac{\sin\theta}{\sin 2\alpha} & 0 & 0 \\ 0 & \frac{1}{2}\cos\theta - \frac{\sin\theta}{\sin 2\alpha} & 0 \\ 0 & 0 & -\cos\theta \end{bmatrix}. \quad (5.9)$$

At $\theta = \pi/2$, where the pressure is smallest, $\alpha = \pi/4$ and the diagonal form is

$$3\mu U \frac{a^3}{r^4} \begin{bmatrix} 1 & 0 & 0 \\ 0 & -1 & 0 \\ 0 & 0 & 0 \end{bmatrix}, \quad (5.10)$$

giving rise to tension and compression.

Following the analysis presented in §2, we next consider the whole stress using (5.2), which may be written as

$$\mathbf{T} + p_c \mathbf{1} = (-p + p_c) \mathbf{1} + 2\mu \nabla \otimes \nabla \phi \quad (5.11)$$

with the addition of the cavitation threshold p_c . After arranging, expression (5.11) becomes

$$\begin{aligned} \frac{\mathbf{T} + p_c \mathbf{1}}{\frac{1}{2}\rho U^2} &= - \left[K + 1 - \left(1 - \frac{a^3}{r^3} \right)^2 \cos^2 \theta - \left(1 + \frac{a^3}{2r^3} \right)^2 \sin^2 \theta \right] \begin{bmatrix} 1 & 0 & 0 \\ 0 & 1 & 0 \\ 0 & 0 & 1 \end{bmatrix} + \\ &+ \frac{3}{Re} \left(\frac{a}{r} \right)^4 \begin{bmatrix} \cos \theta + \frac{2 \sin \theta}{\sin 2\alpha} & 0 & 0 \\ 0 & \cos \theta - \frac{2 \sin \theta}{\sin 2\alpha} & 0 \\ 0 & 0 & -2 \cos \theta \end{bmatrix} \end{aligned} \quad (5.12)$$

where

$$K = \frac{p_\infty - p_c}{\frac{1}{2}\rho U^2} \quad (5.13)$$

is the cavitation number and

$$Re = \frac{\rho U a}{\mu} \quad (5.14)$$

is the Reynolds number.

For the viscous potential flow solution (5.12), one can show that at any point the most tensile (least compressive) and most compressive (least tensile) principal stresses lie in the plane of motion (i.e., the plane where the velocity vector is contained). Suppose now that T_{11} is the largest of the three principal values of stress. Then, according to the maximum tension theory, the locus of the cavitation threshold is given by

$$T_{11} + p_c = 0, \quad (5.15)$$

giving rise to isolines $(a/r, \theta) = f(K_c, Re)$ for the cavitation threshold. The largest values of the viscous irrotational stress are at the boundary $r = a$ where the neglected vorticity is largest. In Appendix A, it is shown that $\theta = 0$ for very low Re and $\theta = \pi/2$ for very high Re are the points most vulnerable for cavitation under the respective conditions.

Equation (5.12) gives the form of the diagonalized stress tensor at each point (r, θ) in the axially symmetric flow. T_{11} , T_{22} and $T_{33} = T_{\varphi\varphi}$ are principal stresses in the principal axes coordinates with bases \mathbf{e}_1 , \mathbf{e}_2 , \mathbf{e}_φ . In the present case, the angle α changes with θ , $\tan 2\alpha = \frac{2}{3} \tan \theta$. The solution of this equation (5.8) is displayed graphically in figure 3. A representation of the orientation of the principal axes in the plane of motion at the surface of the sphere $r = a$ as predicted by (5.8) is presented in figure 4.

It is apparent from (5.12) that the largest stresses are at the boundary of the sphere where $r = a$. Certainly the liquid will cavitate when $K = (p_\infty - p_c) / (\frac{1}{2}\rho U^2) < 0$; only $K > 0$ is of interest. Using now the maximum tension criterion, we see that cavitation occurs for $0 < K < K_c$ and the fluid is most at risk to cavitation for θ at which $K_c(\theta)$ is greatest. For viscous potential flow, this most dangerous θ is at $\theta = 0$ when Re is small and at $\theta = \pi/2$ when Re is large. It follows that the place most at risk to cavitation runs from the rear stagnation point at $\theta = 0$ when Re is small to $\theta = \pi/2$ when Re is large.

In §7 contour plots with lines of constant K representing the cavitation threshold from (5.12) for various Re are presented and compared with the results from the numerical

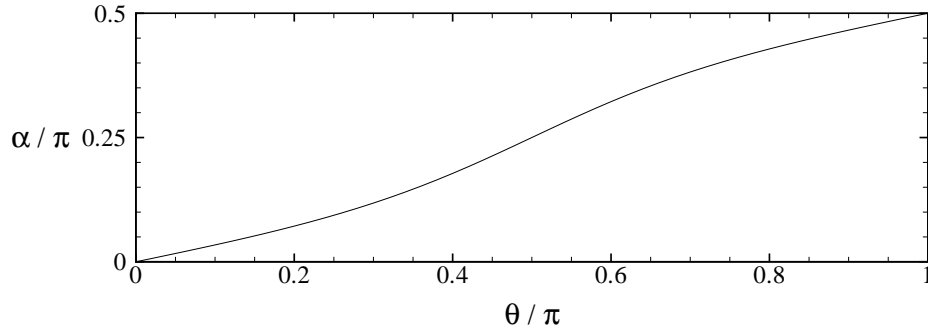


FIGURE 3. Rotation angle α/π versus angular position θ/π , derived from $\tan 2\alpha = \frac{2}{3} \tan \theta$ for irrotational flow of a viscous fluid. A linear approximation of this graph is $\alpha = 0.5\theta$. A cavitation bubble will open asymmetrically with the axis of maximum tension rotated through an angle α at each point r, θ as in this figure.

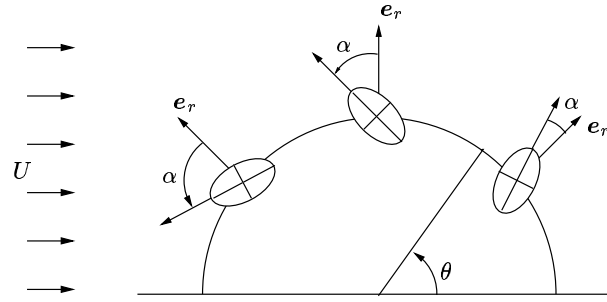


FIGURE 4. Schematic view of the orientation of the principal directions in the plane of motion for irrotational flow of a viscous fluid according to (5.8) on the surface of the sphere. The major axis in the ellipse represents the maximum tensile stress. The angle α puts the direction defined by the unit outward normal vector e_r into the principal direction of the maximum tensile stress.

simulation and the Stokes solution for the lowest Re (see figures 9, 10 and 11). Also, in §7 we have plotted K_c versus θ/π for the three principal stresses at $r = a$ for $Re = 0.01, 10$ and 100 , comparing these results with the corresponding graphs obtained with direct numerical simulation and, for $Re = 0.01$, with the Stokes flow analysis (see figures 12, 13 and 14).

6. Numerical solution of the incompressible Navier–Stokes equations

Numerical investigations of the fundamental aspects of cavitation formation from a wall-stabilized nucleus (Kottke *et al.* 2005 and references therein) or the interaction between the flow field and traveling cavitation bubbles (Kuhn de Chizelle & Brennen 1993) can be encountered in the literature. On the other hand, some effort has been devoted to develop engineering tools based on computational fluid dynamics to model cavitation through different approaches of the multiphase flow (Singhal *et al.* 2002; Farrell, 2003). In this section, the numerical simulation of streaming flow past a sphere is carried out for various values of the Reynolds number Re as defined before. The hydrodynamics is predicted for a single phase, Newtonian, non-cavitating fluid. The velocity and pressure

fields computed in this numerical study are used to determine the principal stresses and directions. Therefore, the cavitation criteria can be formed based on these results and a comparison with the theoretical models from §4 and §5 can be presented.

6.1. Numerical set-up and flow field computations

The numerical solution of the incompressible unsteady Navier–Stokes equations for streaming flow past a sphere is performed using the computational-fluid-dynamics package Fluent® 6.1. This program is based on the finite-volume method which is utilized to integrate the governing equations and then a set of algebraic equations is constructed. An implicit segregated scheme is used to solve the discretized governing equations sequentially. The convective term in the momentum equation is discretized using a Quadratic Upwind Interpolation for Convective Kinematics (QUICK). The pressure–velocity coupling is accomplished through the Pressure-Implicit with Splitting of Operators (PISO) scheme. The time integration of the unsteady momentum equations is carried out using a second-order approximation.

We are interested in the steady-state limit of the solution. The interval for the Reynolds number based on the free-stream velocity U and the radius of the sphere as considered in this simulation is $0 < Re \leq 100$. For this interval of Re , the steady-state-flow motion is described as axisymmetric (see, for instance, Johnson & Patel, 1999). Then, a semi O-type mesh is employed in the numerical simulations. Figure 5 shows a scheme of the computational domain as well as the boundary conditions, where the horizontal edge represents the axis of symmetry and the stream flows from left to right. The outflow boundary condition implies that the diffusion flux in the direction normal to the exit surface is zero for all variables. Therefore, the flow variables at the outflow plane are computed from inside the domain through extrapolation. The interested reader is referred to the Fluent® 6.1's User Guide for details about the numerical schemes and boundary conditions available in the package. Quadrilateral cells in a structured mesh are used to discretize the domain. The position of the outer spherical edge of the computational domain is fixed as $H = 150a$ measured from the center of the sphere. For the selected geometry, the number of cells of the domain is 11680 and the number of nodes is 11907. Using a similar node density, a larger domain was considered by increasing the distance from the center of the sphere to the outer spherical edge ($H = 200a$). The comparison of the drag coefficient computed for these two computational domains indicates that the relative difference is below 1% for $Re = 0.01$ and $Re = 100$. Therefore, we decided to use the mesh with $H = 150a$ to perform further computations. The smallest cells of the domain were located attached to the surface of the sphere and their size increases as the distance from the wall increases. Good resolution of the boundary layer attached to the surface is provided with the selected cells' sizes. The dimensionless time step used in the simulations was $\Delta t U/a = 0.04$. In addition, tests were also conducted with a dimensionless time step of 0.02 and a much finer grid rendering results very close to the previous ones. The initial velocity field is set equal to the free-stream velocity everywhere in the computational domain.

With these settings, computations are performed for different values of the Reynolds number, $Re = 0.01, 10, 25, 50, 75$ and 100 . Therefore, the steady axisymmetric flow conditions reported in the literature from experiments and three-dimensional simulations are expected in all the cases, being consistent with our numerical set-up.

The validation of the numerical setup is carried out by comparing our numerical results for various parameters with results from different sources as compiled and presented in the work of Johnson & Patel (1999). These parameters are the drag coefficient, the separation angle and the separation length. Their definition and the results of the comparison

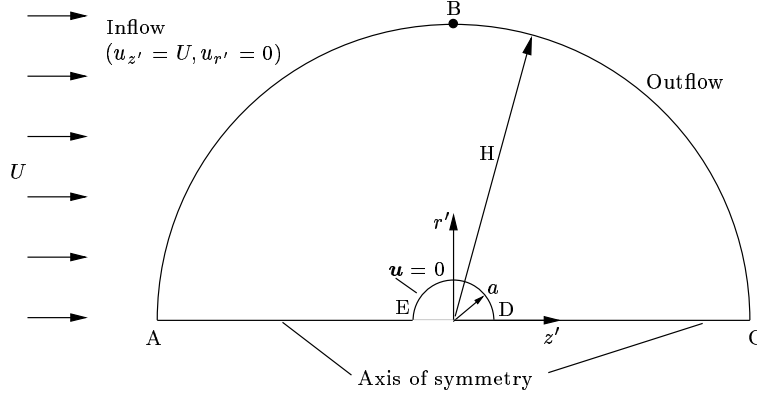


FIGURE 5. Computational domain showing the boundary conditions.

are presented in Appendix B. Satisfactory agreement with previous numerical and experimental results is obtained. Furthermore, the computed flow field is presented in this Appendix through the streamline pattern and contours of vorticity for three values of de Reynolds number.

6.2. Principal stresses and cavitation inception

In order to compute the principal stresses and directions from the velocity and pressure field obtained from the numerical simulations consider the reference frame shown in figure 6 for axysimmetric flow past a sphere. This reference frame is defined by the cylindrical coordinates (z', r', θ') . The corresponding vector basis is defined by the set of unit vectors $\{\mathbf{e}_{z'}, \mathbf{e}_{r'}, \mathbf{e}_{\theta'}\}$. The vector $\mathbf{e}_{\theta'}$ is normal to the page in figure 6(a). The cylindrical coordinates have been used here instead of the spherical polar coordinates utilized in previous sections since the computational solver applied for the direct numerical simulation imposes this system of coordinates for axysimmetric problems with the direction of the axis of symmetry indicated by \mathbf{e}_z' . Therefore, the package computes the derivatives of the components of the velocity with respect to this cylindrical reference frame.

The components of the viscous stress tensor $2\mu\mathbf{D}$ with respect to this set of vectors may be written in matrix form as

$$2\mu \begin{bmatrix} D_{z'z'} & D_{z'r'} & 0 \\ D_{z'r'} & D_{r'r'} & 0 \\ 0 & 0 & D_{\theta'\theta'} \end{bmatrix}, \quad (6.1)$$

where,

$$D_{z'z'} = \frac{\partial u_{z'}}{\partial z'}, \quad D_{r'r'} = \frac{\partial u_{r'}}{\partial r'}, \quad D_{\theta'\theta'} = \frac{u_{r'}}{r'}, \quad D_{z'r'} = \frac{1}{2} \left(\frac{\partial u_{r'}}{\partial z'} + \frac{\partial u_{z'}}{\partial r'} \right) \quad (6.2)$$

and $D_{r'\theta'} = D_{\theta'r'} = D_{z'\theta'} = D_{\theta'z'} = 0$.

The diagonalized form of the stress $2\mu\mathbf{D}$ can be found by rotating the coordinates (z', r') through an angle β such that (6.1) becomes

$$2\mu \begin{bmatrix} \frac{1}{2}(D_{z'z'} + D_{r'r'}) + \frac{D_{z'r'}}{\sin 2\beta} & 0 & 0 \\ 0 & \frac{1}{2}(D_{z'z'} + D_{r'r'}) - \frac{D_{z'r'}}{\sin 2\beta} & 0 \\ 0 & 0 & D_{\theta'\theta'} \end{bmatrix}. \quad (6.3)$$

The rotation angle β such that the direction defined by the unit vector $\mathbf{e}_{r'}$ reaches the

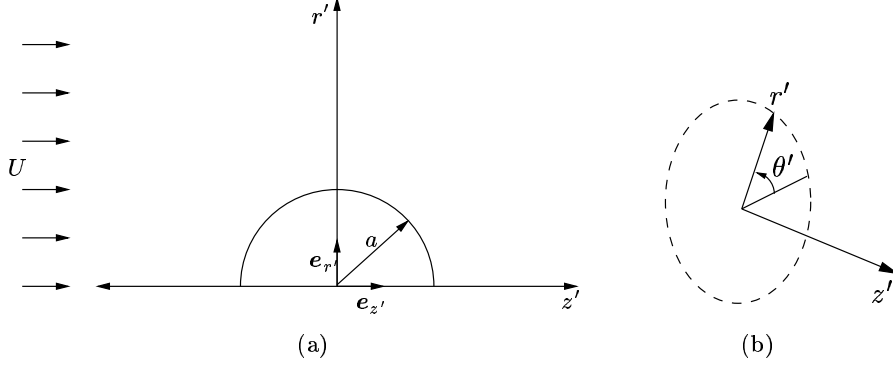


FIGURE 6. Cartoon showing (a) a representation of the axisymmetric flow past a sphere of radius a , and (b) cylindrical coordinates.

principal direction corresponding to the maximum strain-rate in the plane of the fluid motion is related to the components of the strain-rate tensor given in (6.2) according to the expression

$$\tan 2\beta = \frac{2D_{z'r'}}{D_{z'z'} - D_{r'r'}}. \quad (6.4)$$

The angle α associated with the rotation with axis e_φ of the orthogonal reference frame defined by the sphere's outward normal unit vector e_r and the sphere's tangential unit vector e_θ (figure 1) is related to the angle β associated with the rotation with axis $e_{\theta'}$ of the cylindrical coordinates defined by $e_{z'}$ and $e_{r'}$ (figure 6) through the formula

$$\alpha = \beta - \theta. \quad (6.5)$$

The angle α corresponds to the rotation of the spherical polar coordinates (r, θ) in the plane of motion such that the direction of the unit vector e_r coincides with the principal direction associated with the most tensile (or the least compressive) principal stress. The angle α is restricted to the interval $-0.5 \leq \alpha/\pi \leq 0.5$. The rotation angle α/π as a function of the polar angle θ/π on the surface of the sphere $r = a$ is computed from the numerical simulation results and is presented for various Re in figure 7. For $Re = 0.01$ and $Re = 10$ the angle $\alpha = -45^\circ$ coincides with the principal direction of maximum tension for simple shearing. This result was also obtained in the Stokes flow solution and is enforced by the no-slip condition. In the case of $Re = 100$, the angle α shows a similar behavior from the front stagnation point until the point of separation. Beyond this point, the principal axes rotates 90° and the direction of the maximum principal stress is reached for $\alpha = 45^\circ$. Figure 8 presents a cartoon showing the orientation of the principal axes on the plane of motion at different angular positions on the surface of the sphere for $Re = 100$.

Recalling expression (2.1), the total stress tensor for an incompressible Newtonian fluid can be written as

$$\mathbf{T} = -p\mathbf{1} + 2\mu\mathbf{D}.$$

The pressure p can be expressed in terms of the pressure coefficient, which is defined as

$$c_p = \frac{p - p_\infty}{\frac{1}{2}\rho U^2}, \quad (6.6)$$

where p_∞ is a constant reference pressure corresponding to the limiting pressure as

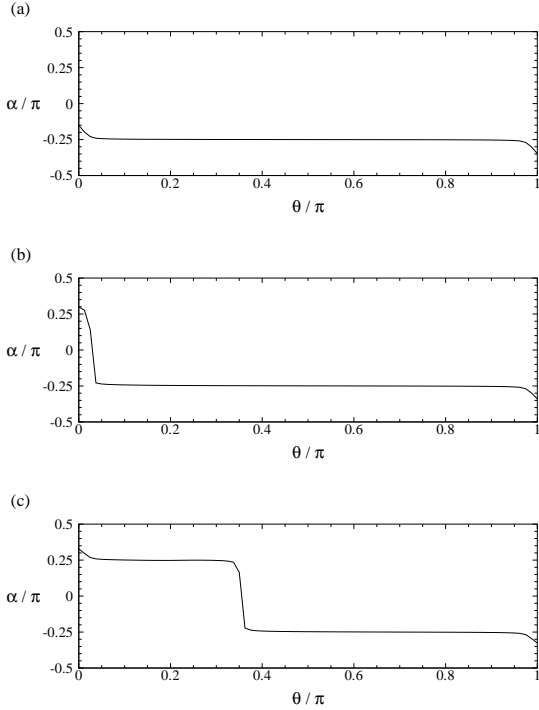


FIGURE 7. Rotation angle α as defined in (6.5) versus θ/π on the surface of the sphere, $r/a=1$, from the numerical solution for (a) $Re=0.01$, (b) $Re=10$, (c) $Re=100$. The position $\theta=0$ corresponds to the rear stagnation point. Notice that for $Re=100$ the jump on the curve occurs at $\theta \approx 63^\circ$, which coincides with the corresponding separation angle θ_s (see figure B.2).

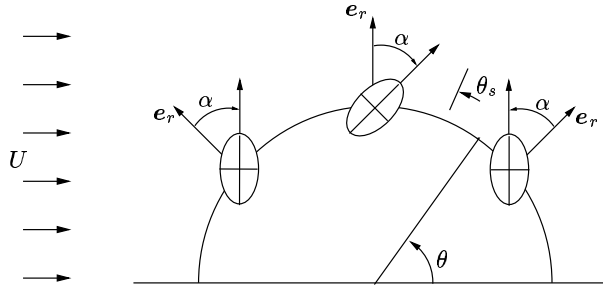


FIGURE 8. Schematic view of the orientation of the principal directions in the plane of motion on the surface of the sphere according to (6.5) from direct numerical simulation of the Navier–Stokes equations and $Re=100$. In this case, $\alpha \approx -45^\circ$ for $\theta > \theta_s$ and $\alpha \approx 45^\circ$ for $\theta < \theta_s$ (from figure 7(c)). The angle θ_s refers to the separation angle measured from the rear stagnation point. The major axis in the ellipse represents the maximum tensile stress. The angle α puts the direction defined by the unit outward normal vector e_r into the principal direction of the maximum tensile stress.

$r \rightarrow \infty$. Then, using (6.6), expression (2.1) becomes,

$$\mathbf{T} = -p_\infty \mathbf{1} - \frac{1}{2} \rho U^2 c_p \mathbf{1} + 2\mu \mathbf{D}. \quad (6.7)$$

Adding $p_c \mathbf{1}$ to both sides of (6.7) yields,

$$\mathbf{T} + p_c \mathbf{1} = -(p_\infty - p_c) \mathbf{1} - \frac{1}{2} \rho U^2 c_p \mathbf{1} + 2\mu \mathbf{D}, \quad (6.8)$$

where p_c is the cavitation threshold. After arranging, (6.8) may be written as

$$\begin{aligned} \frac{\mathbf{T} + p_c \mathbf{1}}{\frac{1}{2} \rho U^2} &= -(K + c_p) \begin{bmatrix} 1 & 0 & 0 \\ 0 & 1 & 0 \\ 0 & 0 & 1 \end{bmatrix} + \\ &+ \frac{4}{Re} \begin{bmatrix} \frac{1}{2} (\tilde{D}_{z'z'} + \tilde{D}_{r'r'}) + \frac{\tilde{D}_{z'r'}}{\sin 2\beta} & 0 & 0 \\ 0 & \frac{1}{2} (\tilde{D}_{z'z'} + \tilde{D}_{r'r'}) - \frac{\tilde{D}_{z'r'}}{\sin 2\beta} & 0 \\ 0 & 0 & \tilde{D}_{\theta'\theta'} \end{bmatrix}, \quad (6.9) \end{aligned}$$

where the dimensionless strain-rate tensor is defined as $\tilde{\mathbf{D}} = \mathbf{D}(a/U)$, and K is the cavitation number as presented in (5.13). The Reynolds number is defined as in (5.14). The principal stresses are thus determined by (6.9).

The velocity field obtained from the numerical solution is used to compute (6.2) and then all the required quantities, including the principal stresses, also utilizing the numerical pressure field. The derivatives of the velocity components in cylindrical coordinates required in (6.2) are approximated by the computational fluid dynamics package using the discrete values of the velocity components obtained from the numerical solution stored at every node.

Consider (6.9) and let T_{11} be the maximum of the principal stresses. Then, the maximum tension criterion (2.6) can be formed. Notice that the maximum principal stress T_{11} may be given by the stress normal to the plane of motion, $T_{\varphi\varphi}$. In the next section, plots of lines of constant K obtained from the numerical simulations corresponding to the cavitation threshold for various Re are presented (figures 9, 10 and 11). In addition, the critical values of the cavitation threshold K_c versus θ/π for the three principal stresses on the surface of the sphere from the numerical results are shown and compared with the viscous potential flow solution and, for a low $Re = 0.01$, with the Stokes flow solution (figures 12, 13 and 14).

7. Discussion

The paper is motivated by the desire to understand the effect of viscosity on stress-induced cavitation of liquids. The study is performed in the framework of direct numerical simulation of the incompressible Navier–Stokes equations to predict the flow field. Analyses are also presented based on the irrotational flow of viscous fluids around a sphere and, for low Reynolds number flows, on the Stokes-flow-limit solution. These formulations allow for a particularly transparent analysis in which all the predictions are given by simple explicit expressions. These formulations relate two dimensionless parameters, the cavitation number associated with the inception of cavitation and the Reynolds number. In the case of the Stokes-flow solution, the formulation is made independent of the Reynolds number by choosing a characteristic viscous-stress scale. The results of this investigation apply to any viscous Newtonian liquid. For all the cases considered, the results from the simplified analytical models are contrasted with the computations from direct numerical simulation.

The main points about stress-induced cavitation, in particular the role of the maximum tensile stress in principal axes coordinates, and the comparison of this criterion with the

criterion depending only on pressure and the most conservative one which requires that all the principal stresses be in tension, are very clearly expressed in the simple analyses based on either viscous potential flow or Stokes flow. In addition, the criteria for cavitation can be neatly formed and evaluated using the velocity and pressure fields from numerical simulations of the governing equations.

Contour plots of lines of constant critical cavitation number K_c from the maximum tension criterion are presented in figures 9, 10 and 11 for $Re = 0.01, 10$ and 100 , respectively. In these figures, the results obtained from the analysis of viscous potential flow and from direct numerical simulation are included. For $Re = 0.01$, the Stokes flow solution is also presented for comparison. Notice that the results from the Stokes limit and the results from direct numerical simulation are very similar, as expected (figures 9 (a) and (c)). The analytical models predict that the risk of cavitation is higher for low Reynolds number flows. This result is confirmed by the numerical experiments. The comparison of the cavitation regions for viscous potential flow and numerical simulation of the Navier–Stokes equations (NS) for $Re = 10$ and 100 is interesting; the cavitation regions shift to the right for NS because of the formation of wakes not present in the irrotational flow solution. As Re increases, the contour plots corresponding to viscous potential flow become symmetric with respect to an axis passing through the center of the sphere, perpendicular to the direction of the free stream velocity, since the contribution of the viscous stress vanishes and the classical “inviscid” potential flow result is approached. As we mentioned, in the case of the numerical solution of NS, the principal stress in the normal direction to the plane of motion may become the largest in some regions of the domain. In such a case, the cavitation inception is determined by this principal stress.

The pressure criterion can readily be presented in dimensionless form as $K_c = -c_p$, in the marginal state separating cavitation from no cavitation. Using the pressure field from the numerical solution of NS equations, contour plots of K_c following the pressure criterion are presented in figures 9 (d), 10 (c) and 11 (c). Comparison of these results with the corresponding results from the maximum tension criterion (figures 9 (c), 10 (b) and 11 (b)) indicates that the latter shifts the region of higher critical cavitation number upstream on the surface of the sphere. The difference is notorious for the lowest $Re = 0.01$. In this case, the region of higher K_c is predicted at 45° from the rear stagnation point by the maximum tension criterion, whereas the pressure criterion indicates that the fluid is at the most risk to cavitation (i.e. maximum K_c) at the rear stagnation point. This result can also be obtained using the pressure field in (4.2) for Stokes flow to define the pressure coefficient c_p . Furthermore, notice that the maximum tension criterion is more conservative than the pressure criterion since $K_{c,\max}$ from the former approach is larger than $K_{c,\max}$ from the latter. As Re increases, both approaches tend to the same distribution since the effects of viscosity carried by the viscous deviator are substantially lessened.

In particular for $r = a$, the surface of the sphere, the profiles of the cavitation number K_c from the maximum tension criterion as a function of θ/π are computed independently for the three principal stresses and presented in figures 12, 13 and 14 for $Re = 0.01, 10$ and 100 , respectively. In each of these figures, the comparison is performed between the VPF solution and the results from the numerical analysis. Also, the predictions from the pressure criterion $K_c = -c_p$, using the numerical solution of NS equations, are presented. For $Re = 0.01$, the results from the Stokes flow limit are included as well. In these figures, T_{11} represents the maximum principal stress and $T_{11} \geq T_{33} \geq T_{22}$. At the surface of the sphere, the pressure criterion coincides with the curve for which $T_{33} + p_c = 0$ because of the no-slip condition. The discrepancies between the predictions from the maximum

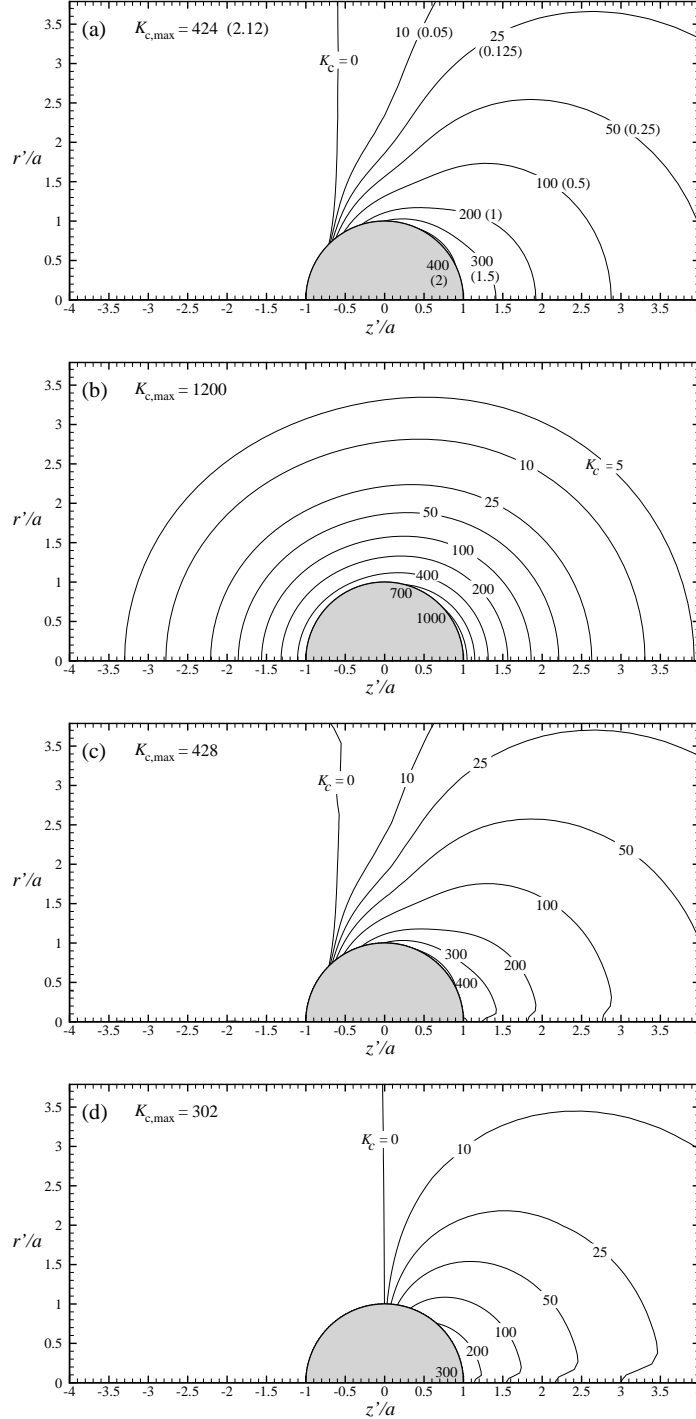


FIGURE 9. Contours of critical cavitation number K_c given by the condition $T_{11} + p_c = 0$ according to the maximum tension criterion for a Reynolds number $Re = 0.01$ from (a) Stokes flow (4.9); (b) the irrotational flow of a viscous fluid (5.12), and (c) numerical solution (6.9); the pressure criterion given by $K_c = -c_p$ is shown in (d) using the numerical pressure field. The cavitation number K is defined in terms of the dynamic pressure $\rho U^2/2$. For a given cavitation number K , cavitation occurs in the region where $K < K_c$. A different normalization of the cavitation number and of the critical cavitation number is used for Stokes flow (4.7) rather than the normalization used for the other cases (5.13). The contour lines for the normalization of $p_\infty - p_c$ with the viscous-stress scale $\mu U/a$ in (4.7) are presented in parenthesis in (a). The ratio of the normalization factors is $Re/2$ (4.10).

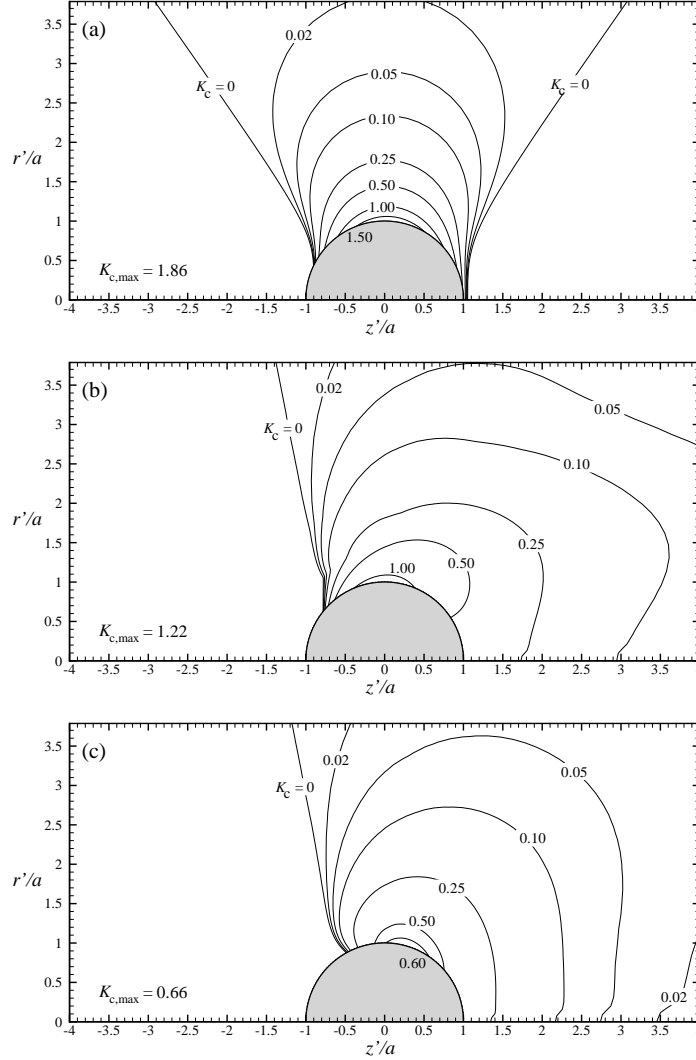


FIGURE 10. Contours of critical cavitation number K_c given by the condition $T_{11} + p_c = 0$ according to the maximum tension criterion for a Reynolds number $Re = 10$ from (a) the irrotational flow of a viscous fluid (5.12), and (b) numerical solution (6.9); the pressure criterion given by $K_c = -c_p$ is shown in (c) using the numerical pressure field. The cavitation number K is defined in terms of the dynamic pressure $\rho U^2/2$. For a given cavitation number K , cavitation occurs in the region where $K < K_c$.

tension criterion and the pressure criterion discussed above are better appreciated when observed at the surface of the sphere, in particular for the lowest $Re = 0.01$ (figure 12 (c)). In this case, the maximum tension criterion predicts the location of the point where K_c is maximum at $\theta = 45^\circ$ using the pressure field from the numerical simulations (the Stokes' approximation yields the same result as shown in Appendix A). With this pressure distribution, the pressure criterion predicts the location of $K_{c,\max}$ at $\theta = 0^\circ$ (the rear stagnation point). The same position is determined from the maximum tension criterion using the pressure field from VPF, though the maximum K_c is much higher in this case (figure 12 (b)). Figures 13 and 14 show that the results from the maximum

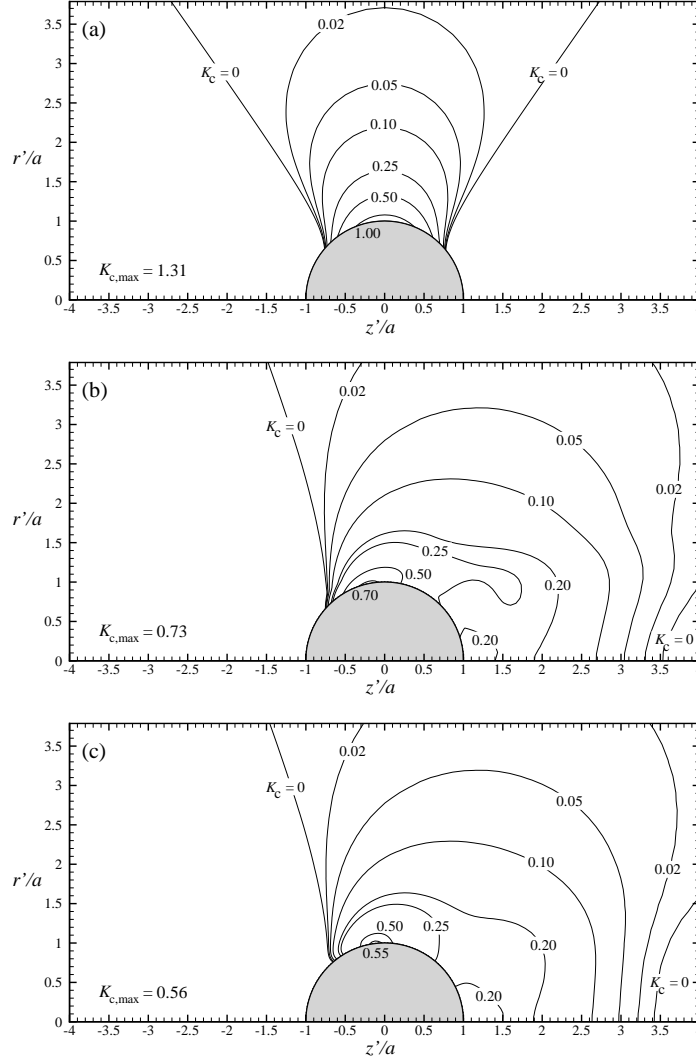


FIGURE 11. Contours of critical cavitation number K_c given by the condition $T_{11} + p_c = 0$ according to the maximum tension criterion for a Reynolds number $Re = 100$ from (a) the irrotational flow of a viscous fluid (5.12), and (b) numerical solution (6.9); the pressure criterion given by $K_c = -c_p$ is shown in (c) using the numerical pressure field. The cavitation number K is defined in terms of the dynamic pressure $\rho U^2/2$. For a given cavitation number K , cavitation occurs in the region where $K < K_c$.

tension criterion tend to the results from the pressure criterion theory for the inception of cavitation as Re increases.

This study has focused on cavitation by homogeneous nucleation. However, important implications are found for heterogeneous nucleation. The results show that the K value is maximized at the surface of the sphere and that viscous normal stresses are important there. This can explain the greater likelihood for heterogeneous nucleation. Furthermore, if the flow around the sphere in figure 1 contained particles that were sufficiently small so that the flow is not modified substantially in a global sense, certain inferences can be made. The normal compressive stress which is locally reduced (or made tensile) by

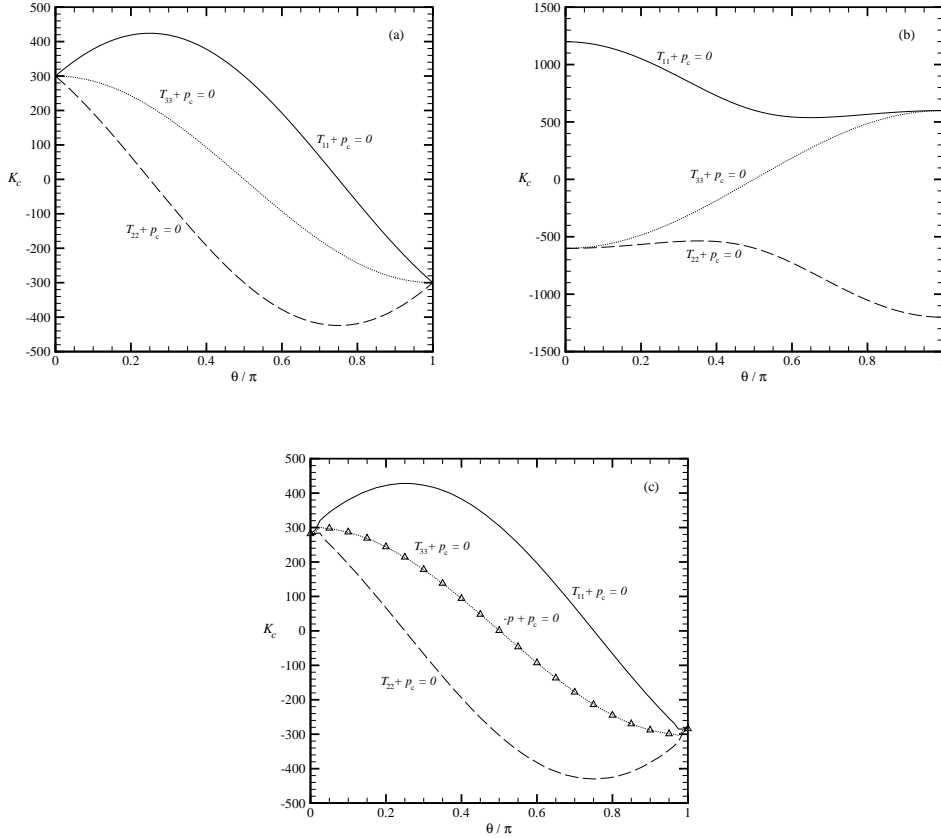


FIGURE 12. Critical cavitation number K_c versus angular position θ/π on the surface of the sphere $r = a$ for $Re = 0.01$ and (a) Stokes flow (4.9); (b) the irrotational flow of a viscous fluid (5.12), and (c) numerical solution (6.9). In addition, the pressure criterion $K_c = -c_p$ has also been included in (c) with the symbol Δ . K_c is defined in terms of the dynamic pressure $\rho U^2/2$. In the figure, three values of the critical cavitation number K_c are determined for every polar angular position θ , with $T_{11} + p_c = 0$, $T_{22} + p_c = 0$ and $T_{33} + p_c = 0$. The position $\theta = 0$ corresponds to the rear stagnation point. For all values of Re , we consider T_{11} as the most tensile principal stress and $T_{11} \geq T_{33} \geq T_{22}$. By multiplying the values in the vertical axis by a factor of $Re/2$, the results for Stokes flow in (a) can be readily presented in terms of the viscous-stress scale $\mu U/a$ instead, according to (4.10).

flow around the sphere can be further reduced due to relative motion between a small particle and the liquid. That is, in a frame of reference fixed to a moving small particle, the liquid will, in some domain, accelerate around and past the small particle, thereby further increasing the local K value when viewed with a finer resolution than we have allowed in our analysis. So, the likelihood of both homogeneous and heterogeneous nucleation is increased by the presence of these small particles.

Irrotational motions of viscous liquids account for viscous stresses but not for vorticity created by the no slip condition at the boundary of solids which is neglected. The analysis is not restricted to small viscosity but is restricted to small vorticity. In steady flows over a sphere the effects of vorticity are greatest in the wake regions behind the separated boundary layers. The irrotational theory cannot be used in the wake region. However,

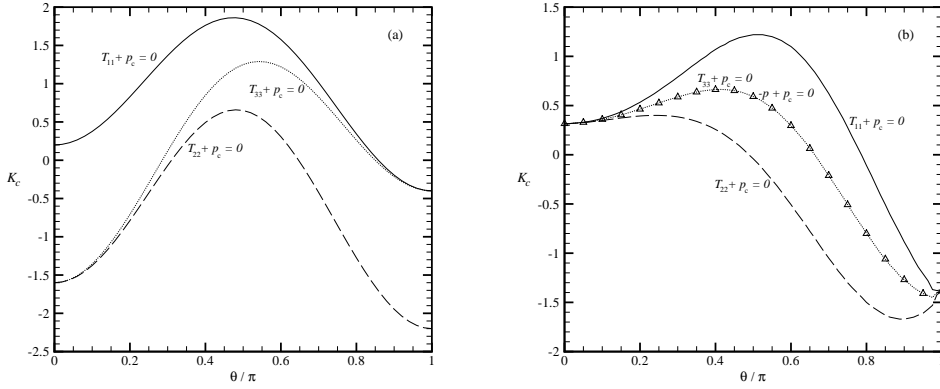


FIGURE 13. Critical cavitation number K_c versus angular position θ/π on the surface of the sphere $r = a$ for $Re = 10$ and (a) the irrotational flow of a viscous fluid (5.12), and (b) numerical solution (6.9). In addition, the pressure criterion $K_c = -c_p$ has also been included in (b) with the symbol Δ . In the figure, three values of the critical cavitation number K_c are determined for every polar angular position θ , with $T_{11} + p_c = 0$, $T_{22} + p_c = 0$ and $T_{33} + p_c = 0$. The position $\theta = 0$ corresponds to the rear stagnation point. For all values of Re , we consider T_{11} as the most tensile principal stress and $T_{11} \geq T_{33} \geq T_{22}$.

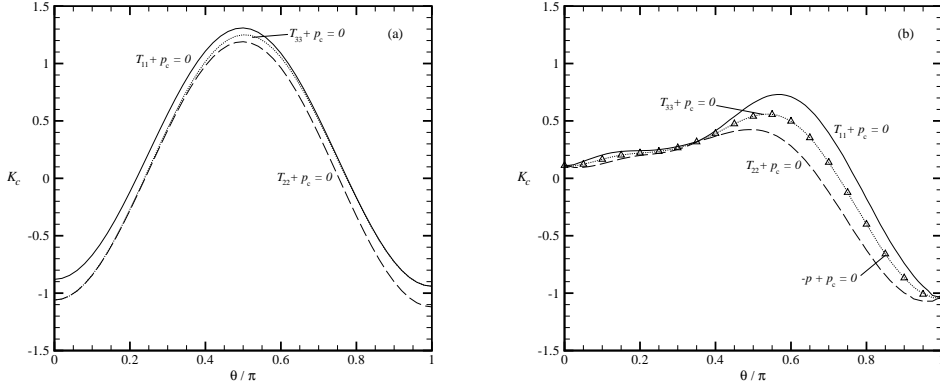


FIGURE 14. Critical cavitation number K_c versus angular position θ/π on the surface of the sphere $r = a$ for $Re = 100$ and (a) the irrotational flow of a viscous fluid (5.12), and (b) numerical solution (6.9). In addition, the pressure criterion $K_c = -c_p$ has also been included in (b) with the symbol Δ . In the figure, three values of the critical cavitation number K_c are determined for every polar angular position θ , with $T_{11} + p_c = 0$, $T_{22} + p_c = 0$ and $T_{33} + p_c = 0$. The position $\theta = 0$ corresponds to the rear stagnation point. For all values of Re , we consider T_{11} as the most tensile principal stress and $T_{11} \geq T_{33} \geq T_{22}$.

this theory predicts that the liquid is at greatest risk to cavitation close to $\theta = 90^\circ$ when Re is high, which is in good agreement with numerical simulation (see figures 13 and 14). Moreover, the cavitation region computed from the irrotational theory is in fair agreement with the numerical simulations with $Re = 10$ and $Re = 100$ for $K > 0.5$ (see figures 10 and 11). On the front face of the sphere including the neighbourhood of the position $\theta = 90^\circ$ we expect a thin boundary layer and an exterior flow closely irrotational for high Reynolds numbers (e.g., $Re = 100$). A good discussion of this can be found in

White (2006). There, it is shown that the skin friction based on the surface velocity of the irrotational flow is close to the actual friction near the front stagnation point and not so hugely different up to the point of separation. The irrotational flow theory given here is off the mark not because the flow is rotational but due to the displacement of the irrotational flow by the separated wake.

The theory of stress-induced cavitation does not require one to assume irrotational flow; we worked the same theory for Stokes flow and Navier-Stokes flow. The predictions for Stokes flow are for very thick fluids creeping around a sphere. We find that the cavities would develop at $\theta = 45^\circ$, at -45° from the direction of shearing. The theory of stress-induced cavitation can be applied to exact numerical simulation, even for turbulent flow.

A clear description of the effects of viscosity in the inception of cavitation was reported by Harvey and collaborators (1947). They carried out experiments of withdrawal of a rod from a liquid container similar to the ones depicted in §3 but using gas-nucleus-free corn syrup (2010 cP and density 1.383 at 23°C) instead of water. Two rods of different materials, aluminum and glass, were drawn from the liquid at a maximum speed of 12.2 m/s. Experiments showed that several minute bubbles formed at the end and side of the rod at the very start of its motion, growing into a long cylindrical bubble. After the rod left the container, the bubble started to collapse. Experiments were repeated for a syrup having viscosity of 56 cP at 25°C and for citrated cat blood plasma, having viscosity slightly greater than water, and no cavities appeared in any case. A maximum rod velocity of 18 m/s was reached in both experiments. These results suggest that cavitation inception presumably induced by the motion of an immersed body is promoted by increasing the liquid viscosity.

As noted by Joseph (1998) the effect of viscosity in cavitation phenomena has been indirectly accounted for through its impact on the structure of the fluid motion, as in the case of separation spots and pressure profiles. For flow past axisymmetric bodies that exhibit laminar boundary layer separation, Arakeri & Acosta (1973) observed that cavitation inception occurs within the region of separated flow. Similarly, Franc & Michel (1985) noticed that detachment of cavities occurs in the recirculation zone, behind laminar boundary layer separation, instead of nearby the point of minimum pressure for flow past circular and elliptical cylinders. Photographs included in the book by Young (1989) for flow past a 1-in-diameter sphere show that inception of cavitation occurs in the shear layer formed between the main stream and the recirculation zone in the wake behind the body. Decreasing the cavitation number associated with the experiment expands the region of cavitation over the surface of the shear layer. By comparing figure B.3 (c) for the streamlines and figure 11 (b) for the critical cavitation number distribution in the case of $Re = 100$, one can conjecture, on qualitative grounds, that cavitation events may be generated as traveling nuclei pass through the region of high K_c (the equator of the sphere), where their growth is triggered, and immediately enter the shear layer region carried by the external flow, while becoming visible to the unaided eye. Inside the recirculation zone, the higher values of the critical cavitation number occur in the neighbourhood of the point of boundary layer separation (about $\theta = 60^\circ$; see figures B.2 (b) and B.3 (c)), which is also a low velocity region. Thus, it seems likely that cavities become visible in this region of the wake.

Liu & Brennen (1998) studied traveling bubble cavitation for water flow over a Schiebe headform. Free-stream gas nuclei grow to become macroscopic bubbles as they travel through the low-pressure region close to the surface of the blunt body and then collapse, describing a typical cavitation event. Liu & Brennen noticed that, for low air content, attached cavitation occurs immediately after traveling bubble cavitation. The cause for

the opening of an attached cavity is not clear since no laminar boundary layer separation appeared on the Schiebe headform in the low pressure region. One can think of the growth of a cavity on the surface of the body driven by the stresses created in the flow.

The main prediction of this work is that highly viscous fluids are at greater risk to cavitation at a fixed cavitation number. This prediction appears to be new since the question seems, surprisingly, not to have been addressed in the theoretical cavitation literature.

The work of J.C. Padrino and D.D. Joseph was partially supported by a grant 0302837 from the National Science Foundation. We wish to thank Prof. Roger Arndt for useful suggestions regarding the scaling for Stokes flow. We also acknowledge the University of Minnesota Supercomputer Institute for supporting the numerical work by providing the computational fluid dynamics package and computer time. We also kindly acknowledge the suggestions and inquiries from the referees which have substantially enriched the presentation and discussion of results.

REFERENCES

- APPFEL, R.E. 1970 The role of impurities in cavitation-threshold determination. *J. Acoust. Soc. Am.* **48**, 1180–1186.
- ARAKERI, V.H. & ACOSTA, A.J. 1973 Viscous effects in the inception of cavitation on axisymmetric bodies. *J. Fluids Eng.* **95**, 519–527.
- ARCHER, L.A., TERNET, D. & LARSON, R.G. 1997 'Fracture' phenomena in shearing flow of viscous liquids. *Rheol. Acta* **36**, 579–584.
- ASHMORE, J., DEL PINO, C. & MULLIN, T 2005 Cavitation in a lubrication flow between a moving sphere and a boundary. *Phys. Rev. Lett.* **94**, 124501.
- BAIR, S. & WINER, W.O. 1990 The high shear stress rheology of liquid lubricants at pressure of 2 to 200 MPa. *J. Tribol.* **114**, 246–253.
- BAIR, S. & WINER, W.O. 1992 The high pressure high shear stress rheology of liquid lubricants. *J. Tribol.* **114**, 1–13.
- BILLET, M.L. 1985 Cavitation nuclei measurements—A review. *ASME Cavitation and Multiphase Flow Forum-1985*, ASME, New York, FED **23**, 31–38.
- BLAKE, J.R. & GIBSON, D.C. 1987 Cavitation bubbles near boundaries. *Ann. Rev. Fluid Mech.* **19**, 99–123.
- BRIGGS, L.J. 1950 Limiting negative pressure of water. *J. Appl. Phys.* **21**, 721–722.
- CHEN, Y. & ISRAELACHVILI, J. 1991 New mechanism of cavitation damage. *Science* **252**, 1157–1160.
- CRUM, L.A. 1982 Nucleation and stabilization of microbubbles in liquids. *Appl. Sci. Res.* **38**, 101–115.
- FARRELL, K.J. 2003 Eulerian/Lagrangian analysis for the prediction of cavitation inception. *J. Fluids Eng.* **125**, 46–52.
- FRANC, J. P. & MICHEL, J. M. 1985 Attached cavitation and the boundary layer; experimental investigation and numerical treatment. *J. Fluid Mech.* **154**, 63–90.
- FISHER, J.C. 1948 The fracture of liquids. *J. Appl. Phys.* **19**, 1062–1067.
- Fluent 6.1. 2003 User's Guide. Fluent Inc. Lebanon, NH.
- FOTEINOPOLOU, K., MAVRANTZAS, V. G. & TSAMOPOULOS, J. 2004 Numerical simulation of bubble growth in Newtonian and viscoelastic filaments undergoing stretching. *J. Non-Newtonian Fluid Mech.* **122**, 177–200.
- FUNADA, T., WANG, J. & JOSEPH, D. D. 2006 Viscous potential flow analysis of stress induced cavitation of aperture flow. *Atomization and Sprays*, submitted.
- HARVEY, E.N., BARNE, D.K., MC ELROY, W.D., WHITELEY, A. H., PEASE, D.C. & COOPER, K.W. 1944a Bubble formation in animals, I. Physical factors. *J. Cell. Comp. Physiol.* **44**, 1–22.
- HARVEY, E.N., WHITELEY, A.H., MC ELROY, W.D., PEASE, D.C. & BARNE, D.K. 1944b

- Bubble formation in animals, II. Gas nuvlei and their distribution in blood and tissues. *J. Cell. Comp. Physiol.* **44**, 23–34
- HARVEY, E.N., MC ELROY, W.D. & WHITELEY, A. H. 1947 On cavity formation in water. *J. Appl. Phys.* **18**, 162–172.
- JOHNSON, T. A. & PATEL, V. C. 1999 Flow past a sphere up to a Reynolds number of 300. *J. Fluid Mech.* **378**, 19–70.
- JOSEPH, D. D. 1995 Cavitation in a flowing liquid. *Physical Review E*, **51**(3), R1649–1650.
- JOSEPH, D. D. 1998 Cavitation and the state of stress in a flowing liquid. *J. Fluid Mech.* **366**, 367–378.
- JOSEPH, D. D. & LIAO, T. Y. 1994 Potential flows of viscous and viscoelastic fluids. *J. Fluid Mech.* **265**, 1–23.
- KNAPP, R.T. 1958 Cavitation and nuclei. *Trans. ASME* **80**, 1315–1324.
- KNAPP, R.T., DAILY, J.W. & HAMMIT, F.G. 1970 Cavitation. McGraw-Hill, Inc.
- KOTTKE, P.A., BAIR, S. & WINER, W.O. 2003 The measurement of viscosity of liquids under tension. *J. Tribol.* **125**, 260–266.
- KOTTKE, P.A., BAIR, S. & WINER, W.O. 2005 Cavitation in creeping shear flows. *AICHE J.* **51**, 2150–2170.
- KUHL, T., RUTHS, M., CHEN, Y., & ISRAELACHVILI, J. 1994 Direct visualization of cavitation and damage in ultrathin liquid films. *J. Heart Valve Disease* **3**, 117–127.
- KUHN DE CHIZELLE, Y. & BRENNEN, C.E. 1993 Comparison of observed and calculated shapes of travelling cavitation bubbles. *Proc. IUTAM Symp. on Bubble Dynamics and Interface Phenomena, Birmingham, UK*. 207–217.
- KUHN DE CHIZELLE, Y., CECCIO, S.L. & BRENNEN, C.E. 1995 Observation and scaling of travelling bubble cavitation. *J. Fluid Mech.* **293** 99–126.
- LIU, Z. & BRENNEN, C. E. 1998 Cavitation nuclei population and event rates. *J. Fluids Eng.* **120**, 728–737.
- MAGNAUDET, J., RIVERO, M. & FABRE, J. 1995 Accelerated flows past a rigid sphere or a spherical bubble. Part 1. Steady straining flow . *J. Fluid Mech.* **284**, 97–135.
- PEREIRA, A., MCGRATH, G. & JOSEPH, D.D. 2001 Flow and stress induced cavitation in a journal bearing with axial throughput. *J. Tribol.* **123**, 742–754.
- PLESSET, M. 1969 Tensile strength of liquids. *Office of Naval Res. Rep.* 85–4.
- PRUPPACHER, H. R., LE CLAIR, B. P. & HAMILIEC, A. E. 1970 Some relations between drag and flow pattern of viscous flow past a sphere and a cylinder at low an intermediate Reynolds numbers. *J. Fluid Mech.*, **44**, 781.
- ROOS, F. W. & WILLMARTH, W. W. 1971 Some experimental results on sphere and disk drag. *AIAA J.* **9**, 285–291.
- SINGHAL, A. K., ATHAVALE, M. M., LI, H. & JIANG, Y. 2002 Mathematical basis and validation of the full cavitation model. *J. Fluids Eng.* **124**, 617–624.
- STRASBERG, M. 1959 Onset of ultrasonic cavitation in tap water. *J. Acoust. Soc. Am.* **31**, 163–176.
- TANEDA, S. 1956 Experimental investigation of the wake behind a sphere at low Reynolds numbers.. *J. Phys. Soc. Japan* **11**, 1104–1108.
- TOMBOULIDES, A. G. 1993 Direct and large-eddy simulation of wake flows: flow past a sphere. PhD thesis, Princeton University.
- WHITE, F. K. 2006 *Viscous fluid flow*. 3rd. ed., McGraw-Hill, section 4-10-4, p. 294-5.
- WINER, W.O. & BAIR, S. 1987 The influence of ambient pressure on the apparent shear thinning of liquid lubricants—an overlooked phenomena. Conference Publication 1987-5. Vol. 1. London: Inst. Mech. Eng. C190-87, 395–398.
- YOUNG, F.R. 1989 *Cavitation*. McGraw-Hill, Inc.

Appendix A. An analysis for maximum K

Here we look for the angular position on the surface of the sphere at which the maximum value of the cavitation number K occurs. This position is the most vulnerable to cavitation.

For the potential flow solution, the stress tensor is given in (5.12). Suppose that T_{11} is

the maximum tensile stress such that $T_{11} \geq T_{33} \geq T_{22}$. If we consider the surface of the sphere $r = a$ and use the cavitation criterion $T_{11} + p_c = 0$, we obtain from (5.12)

$$K = \frac{9}{4}\sin^2\theta - 1 + \frac{3}{Re} \left(\cos\theta + \frac{2\sin\theta}{\sin 2\alpha} \right), \quad (\text{A.1})$$

Considering the expression for α given in (5.8)

$$\tan 2\alpha = \frac{2}{3}\tan\theta, \quad (\text{A.2})$$

we can write (A.1) as

$$K = \frac{9}{4}\sin^2\theta - 1 + \frac{3}{Re} \left[\cos\theta + 3\cos\theta \sqrt{1 + \frac{4}{9}\tan^2\theta} \right], \quad (\text{A.3})$$

for $0 \leq \theta \leq \pi/2$, whereas

$$K = \frac{9}{4}\sin^2\theta - 1 + \frac{3}{Re} \left[\cos\theta - 3\cos\theta \sqrt{1 + \frac{4}{9}\tan^2\theta} \right], \quad (\text{A.4})$$

for $\pi/2 < \theta \leq \pi$. Taking the derivative of K in (A.3), we find

$$\frac{\partial K}{\partial \theta} = \frac{9}{2}\sin\theta\cos\theta - \frac{3}{Re}\sin\theta \left[1 + \frac{5}{\sqrt{9 + 4\tan^2\theta}} \right]. \quad (\text{A.5})$$

It is obvious that $\theta = 0$ is a solution of $\partial K / \partial \theta = 0$ at any Reynolds number. We compute $\partial^2 K / \partial \theta^2$ to determine whether K at $\theta = 0$ is a local maximum or minimum. From (A.5), the second derivative of K is

$$\frac{\partial^2 K}{\partial \theta^2} = \frac{9}{2}\cos 2\theta + \frac{60 \sec \theta \tan^2 \theta}{Re (9 + 4\tan^2\theta)^{3/2}} - \frac{\cos\theta}{Re} \left(3 + \frac{15}{\sqrt{9 + 4\tan^2\theta}} \right). \quad (\text{A.6})$$

When $\theta = 0$, we have

$$\frac{\partial^2 K}{\partial \theta^2}(\theta = 0) = \frac{9}{2} - \frac{8}{Re}. \quad (\text{A.7})$$

Thus $\partial^2 K / \partial \theta^2$ at $\theta = 0$ is negative when $Re < 16/9$ and positive when $Re > 16/9$. This result indicates that K at $\theta = 0$ is a local maximum when $Re < 16/9$ and is a local minimum when $Re > 16/9$. Substitution of $\theta = 0$ in (A.3) yields

$$K(\theta = 0) = \frac{12}{Re} - 1, \quad (\text{A.8})$$

which is a local maximum of K for $Re < 16/9$ in the interval $0 \leq \theta \leq \pi/2$.

Besides $\theta = 0$, there is a second solution for $\partial K / \partial \theta = 0$ which depends on Re and has a very complicated expression. If the value of Re is very high, then $\partial K / \partial \theta \approx 9\sin(2\theta)/4$. The second solution is close to $\theta = \pi/2$. We also notice that $\partial^2 K / \partial \theta^2 < 0$ at $\theta = \pi/2$ when Re is high. Therefore, the maximum value of K occurs near $\theta = \pi/2$ when Re is high in the interval $0 \leq \theta \leq \pi/2$.

Similarly, from (A.4), K has a local maximum at $\theta = \pi$ when $Re < 4/9$ and has a local minimum at this position when $Re > 4/9$ in the interval $\pi/2 < \theta \leq \pi$. Substitution of $\theta = \pi$ into (A.4) gives this local maximum for $Re < 4/9$ in the interval $\pi/2 < \theta \leq \pi$,

$$K(\theta = \pi) = \frac{6}{Re} - 1. \quad (\text{A.9})$$

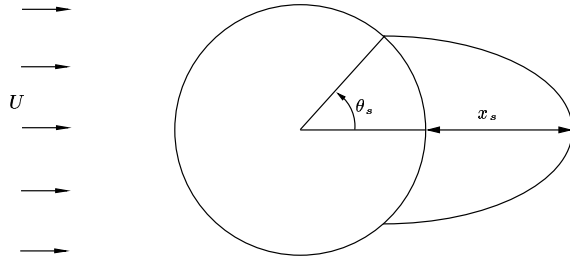


FIGURE B.1. Sketch showing two geometric parameters of the axisymmetric flow past a sphere: polar separation angle θ_s and separation length x_s .

A second solution, as a complicated function of Re , can be written for $\partial K/\partial\theta = 0$. For high Re , this solution gives that K goes to a maximum when θ approaches $\pi/2$.

A comparison of (A.8) and (A.9) allows us to discard the position $\theta = \pi$. Summarizing our findings for viscous potential flow, K reaches a maximum at $\theta = 0$ when $Re < 16/9$ in the interval of interest $0 \leq \theta \leq \pi$. In addition, in the limit of high Re , K is maximum at $\theta = \pi/2$ in this interval. These results are verified in figures 9 (b) and 12 (b) for low Re and figures 11 (a) and 14 (a) for high Re .

For the Stokes flow solution, the stress tensor on the surface of the sphere is given in (4.12). With $T_{11} + p_c = 0$, we obtain

$$K = \frac{3}{2}(\cos\theta + \sin\theta). \quad (\text{A.10})$$

The maximum K occurs at $\theta = \pi/4$ or 45° . Thus $\theta = 45^\circ$ is the location most vulnerable to cavitation on the surface of the sphere. This result is illustrated in figures 9 (a) and 12 (a) when $Re = 0.01$.

Appendix B. Validation of the numerical setup

The numerical strategy implemented in this work is validated by comparing our results with those from various publications collected by Johnson & Patel (1999). The evaluation is performed in terms of the drag coefficient and two relevant geometric parameters of the flow, namely, the separation angle θ_s and the separation length x_s as a function of the Reynolds number Re . The separation angle θ_s represents the angle, measured from the rear stagnation point, where the flow separates from the sphere. The separation length x_s represents the distance along the axis of symmetry, measured from the rear stagnation point, where the separated flow rejoins. These two parameters, the separation angle and length, are described in figure B.1. The drag coefficient is defined as:

$$C_D = \frac{F_{z'}}{\frac{1}{2}\rho U^2 \pi a^2} \quad (\text{B.1})$$

where $F_{z'}$ represents the force that the fluid motion produces on the body in the streamwise direction.

The data considered in this study embraces the experimental results of Taneda (1956) and the numerical results of Pruppacher, Le Clair & Hamilie (1970), Tomboulides (1993) and Magnaudet, Rivero & Fabre (1995). In addition, the results presented by Roos & Willmarth (1971) as well as the data owed to Johnson & Patel (1999) are included. Excellent agreement between our numerical values and the corresponding results from the literature is observed in figure B.2.

Once the velocity field has been determined from the numerical solution of the gov-

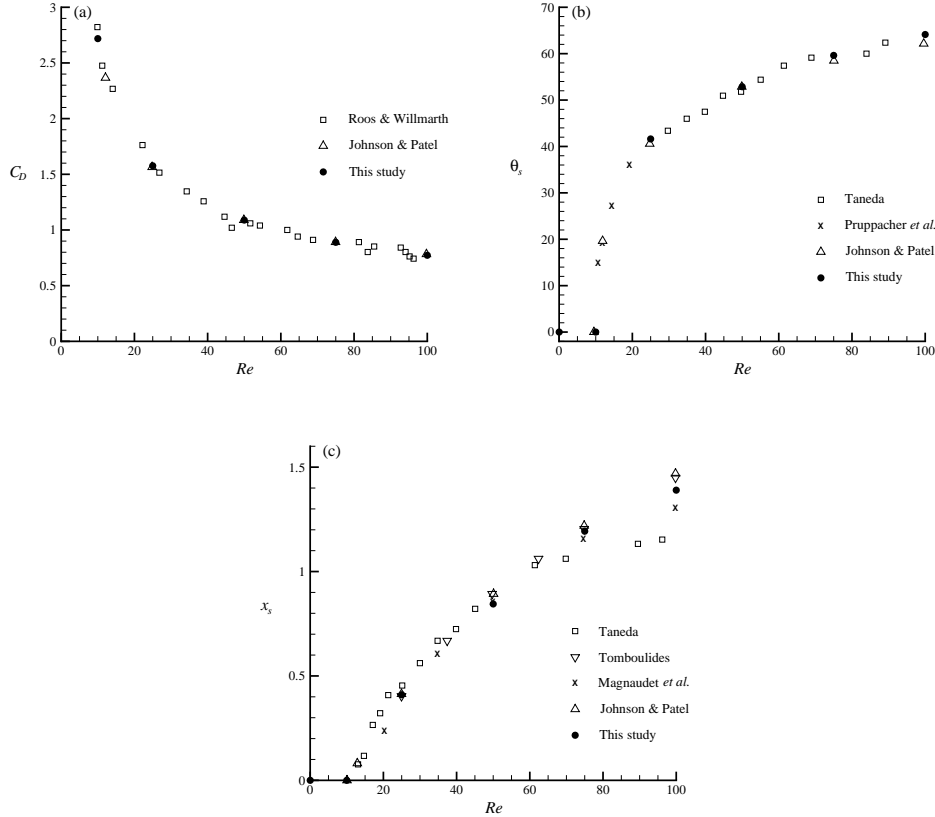


FIGURE B.2. Comparison between the numerical results from this study with data from the literature: (a) Drag coefficient C_D ; (b) polar separation angle θ_s (is zero at the rear stagnation point), and (c) separation length x_s versus Re . All the data from previous works is extracted from the paper of Johnson & Patel (1999).

erning equations, the stream function and vorticity fields can be computed by the computational fluid dynamics package using the velocity components known at every node. The stream function is expressed in terms of the connection between conservation of mass and the definition of streamlines. Since a streamline is determined by a constant value of the stream function, the mass rate of flow between two streamlines is given by the difference of the stream function's values corresponding to these streamlines (Fluent 6.1 User's Guide, 2003). Figure B.3 presents the streamlines for streaming flow past a sphere for $Re = 0.01, 10$ and 100 . For the former case, the classic symmetric pattern with respect to the equator of the sphere ($\theta = \pi/2$) is observed. As Re increases, this symmetry disappears and the separation of the laminar boundary layer for $Re = 10$ is about to occur (Johnson & Patel, 1999). For $Re = 100$, separation has taken place and a well defined stable axisymmetric recirculation region is formed behind the sphere. For $Re = 0.01, 10$ and 100 , the vorticity contours $\omega a/U$ are presented in figure B.4. For the lower Re , the diffusion of vorticity prevails and the levels of vorticity show symmetry with respect to the axis $\theta = \pi/2$. For $Re = 10$ and $Re = 100$ the vorticity is convected by the fluid motion.

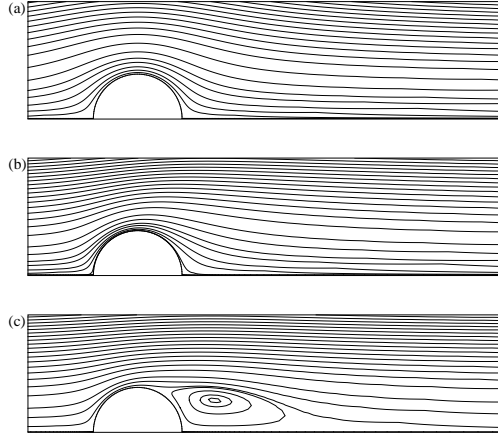


FIGURE B.3. Streamline pattern ψ/aU^2 for streaming flow past a sphere from the numerical solution for various Reynolds numbers; (a) $Re = 0.01$, (b) $Re = 10$, (c) $Re = 100$. The streamline $\psi = 0$ corresponds to the axis of symmetry and the sphere's surface.

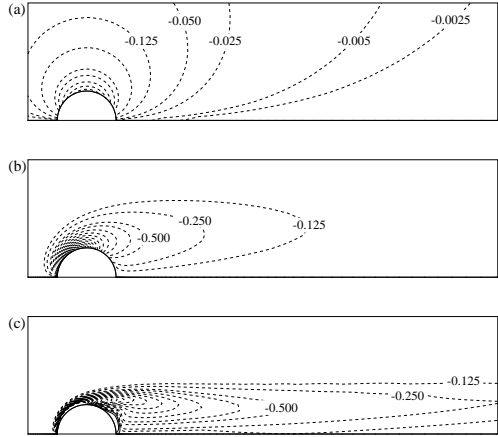


FIGURE B.4. Vorticity contours $\omega a/U$ for various Re from the numerical solution. (a) $Re = 0.01$, (b) $Re = 10$, (c) $Re = 100$. The solid lines (for $Re = 100$) represent contours of positive vorticity.